Breaching of the Sillon de Talbert gravel spit (North Brittany, France) and coastal flooding risk assessment

Pierre Stéphan, Serge Suanez, Thomas Guérin, Aurélie Rivier, Laurent Leballeur, Benoit Waeles, Jérôme Ammann, Julien Houron

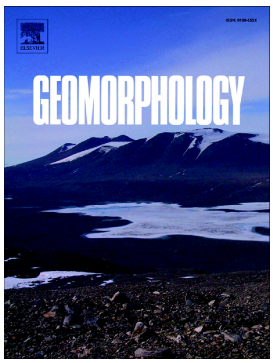

Breaching of the Sillon de Talbert gravel spit (North Brittany, France) and coastal flooding risk assessment

Pierre Stéphan, Serge Suanez, Thomas Guérin, Aurélie Rivier, Laurent Leballeur, Benoit Waeles, Jérôme Ammann, Julien Houron

PII: S0169-555X(24)00252-6

DOI: https://doi.org/10.1016/j.geomorph.2024.109302

Reference: GEOMOR 109302

To appear in: *Geomorphology*

Received date: 19 December 2023

Revised date: 6 June 2024

Accepted date: 6 June 2024

Please cite this article as: P. Stéphan, S. Suanez, T. Guérin, et al., Breaching of the Sillon de Talbert gravel spit (North Brittany, France) and coastal flooding risk assessment, *Geomorphology* (2023), https://doi.org/10.1016/j.geomorph.2024.109302

Breaching of the Sillon de Talbert gravel spit (North Brittany, France) and coastal flooding risk assessment

Pierre Stéphan [a], Serge Suanez [b*], Thomas Guérin [c], Aurélie Rivier [d], Laurent Leballeur [d], Benoit Waeles [c], Jérôme Ammann [e], Julien Houron [f]

[a] CNRS, Univ Brest, UMR LETG 6554, Institut Universitaire Européen de la Mer, F-29280 Plouzané, France

[b] Univ Brest, CNRS, UMR LETG 6554, Institut Universitaire Européen de la Mer, F-29280 Plouzané, France

[c] Waeles Marine Consultants, 53 rue du commandant Groix, 29200 Brest, France

[d] Actimar SAS, 36, quai de la Douane, 29200 Brest, France

[e] CNRS, Univ Brest, UMR LGO 6538, Institut Universitaire Européen de la Mer, Plouzané, France

[f] Réserve Naturelle Régionale du Sillon de Talbert, 22610 Pleubian, France

[*] Corresponding authors: serge.suanez@univ-brest.fr (S. Suanez) +33 (0)2 98 49 86 10 (ORCID : 0000-0003-0872-8699)

pierre.stéphan@univ-brest.fr (P. Stéphan) - ORCID : 0000-0001-7975-2149

thomas.guerin@bw-cgc.fr (T. Guérin) - ORCID : 0000-0002-2897-3117

aurelie.rivier@actimar.fr (A. Rivier) - ORCID : 0000-0002-5521-3957

Laurent.leballeur@shom.fr (L. Leballeur) - ORCID : 0009-0003-5085-6843

benoit.waeles@bw-cgc.fr (B. Waeles)

Jerome.Ammann@univ-brest.fr (J. Ammann) - ORCID : 0000-0002-2574-9849

garde.littoral@mairie-pleubian.fr (J. Houron)

Abstract

Coastal barriers are a natural defence against the marine submersion of low-lying back-barrier areas. In March 2018, a breach opened up in the proximal section of the Sillon de Talbert spit barrier (North Brittany, France), causing great concern among local residents and elected representatives. A study to assess the risk of submersion of the low-lying areas of the Laneros Peninsula, located behind the barrier, was carried out in 2020. Hydrodynamic conditions (waves, currents, and water levels) were modeled using Telemac-2D coupled with the phase-averaged wave model TOMAWAC. Simulations were compiled for the storm of February 1, 2014, corresponding to the most morphogenic event to occur in the last two decades. Five topomorphological configurations were considered for the numerical simulations: configurations #1 and #2 correspond to the ante-breach and post-breach morphological settings, while configurations #3, #4, and #5 correspond to hypothetical scenarios, from the

enlargement of the breach (from 300 to 500 m width), to complete crest lowering of the barrier after a complete removing of the crest due to catastrophic overwash events. The results show that the breach accelerates the draining of the back-barrier sandflat, thereby reducing the height of extreme water levels at the coastline. This is mainly due to different tidal impacts on either side of the barrier, with a higher water level and the tidal peak occurring 15 minutes later and the on the back-barrier than on the ocean-side zone. As a result, ebb currents begin to flow before the high tide level is reached, inducing a significant draining with a lowering of the extreme water level at the back-barrier zone. However, these simulations do not take into account the effects of climate change over the coming years, in particular the future rise in sea level and/or the acceleration of erosion processes already underway.

Keywords: Gravel spit; breach; flooding risk; modelling; coastal management, Brittany

1. Introduction

Coastal barriers provide an effective coastal defence for the low-lying back-barrier areas (Schoonees et al., 1998; Hartley and Pontee, 2008; Pye and Blott, 2009; Dornbusch, 2017). Therefore, they act as natural coastal protection feature since they may significantly dissipate energetic storm wave energy related to overwash and flooding hazards (Plomaritis et al., 2018; Pollard et al., 2021). Coastal barriers (including barrier-spits and barrier-islands) are widely spread along the world's coastline. While they are mainly composed of sand, a few proportion of gravel-dominated barriers are concentrated in formerly glaciated areas in mid- and upper-latitudes (Forbes et al., 1995; Orford et al., 1995, 2002). Due to the steep beach sea-face related to the coarse sediments composing these coastal landforms, gravel barrier morphodynamics are mainly dominated by highly reflective processes (Carter and Orford, 1984; Jennings and Shulmeister, 2002; Buscombe and Masselink, 2006), and occasionally by infragravity waves (Bertin et al., 2018; Billson et al., 2019). Therefore, during storm wave conditions, energetic swash motions generated by waves breaking close to -and/or on- the lower beach face induce frequent overtopping/overwashing of the barrier crest (Carter and Orford, 1981; Poate et al., 2013; Almeida et al., 2015).

For swash-aligned barriers, overtopping to overwashing processes affecting gravel barriers mainly occur during extreme storm conditions. However, according to the storm-impact scaling model of Orford and Carter (1982), the morphological responses of the barriers to storm impact are ranged into four distinct regimes: *(i) swash overtopping* inducing crest

raising, *(ii) discrete overwash* inducing crest lowering, *(iii) sluicing overwash* inducing barrier landward migration through rollover, and *(iv)* exceptionally *catastrophic overwash* inducing barrier breaching. These different barrier responses to storm events are controlled by the elevation difference between the extreme water level (including runup) and the barrier crest, which is known as *freeboard* (Orford and Anthony, 2011). When the extreme water level does not exceed the crest height (*i.e.*, positive *freeboard*), regime of energetic swash processes induce the raising of the barrier. In contrast, as the extreme water level starts to exceed the crest height (*i.e.*, negative freeboard), the top of barrier starts to erode and sediments are displaced to the back-barrier slope. As the extreme water level and swash flows increase even more, overtopping is replaced by catastrophic overwashing that may open a breach along the barrier (Orford and Carter, 1995).

The breaching process also impacts the drift-aligned barriers, which are very sensitive to longshore sediment supply (Orford et al., 1991). The scarcity of sediment generally induces an erosion of the barrier in the updrift (proximal) zone. Along the barrier, selective sediment transports tend to lead to the formation of distinct erosion/accretion cells, and even sub-cells. Within each cell or sub-cell, sediment is eroded updrift to be accumulated downdrift (sink zone) where the shoreline is prograding. With time, these processes lead to a thinning of the updrift eroded zone (weaker point), eventually resulting in a breaching of the barrier (Orford et al., 1996).

The study of sandy- and gravel-dominated barrier breaching processes and the related environmental and socio-economic consequences has been the subject of numerous studies (Kraus and Wamsley, 2003; Wamsley and Kraus, 2005; Stockdon et al., 2007; Dornbusch, 2017; Plomaritis et al., 2018). The East and Gulf Coasts of the United States (*i.e.*, from Florida to New York States), which are regularly impacted by severe hurricanes, have clearly been the most studied areas in the world for barrier breaches, particularly those of barrier-islands (Plant et al., 2010; Plant and Stockdon, 2012; Stockdon et al., 2012, 2013). In natural areas with no human settlements, the consequences are essentially environmental due to the modification of hydrologic exchanges between the sea and the back-barrier lagoons (Kraus *et al.*, 2002). These modifications can result in increased water levels linked to the inflow of marine water (Elsayed and Oumeraci, 2016), inducing saltwater intrusion to the deeper freshwater aquifers (Elsayed and Oumeraci, 2018). Under these conditions, the biodiversity of the coastal wetland ecosystem is affected by the changes in the salinity of the surface water (Li et al., 2020). In terms of morphological features, overwashing flows causing erosion and barrier breaching generally lead to inlet formation (Leatherman, 1979a; Nienhuis et al., 2021).

The removed sediments can then be deposited and form washover fans (Leatherman, 1979b; Carter and Orford, 1981, 1984). However, the most significant risk generated by the opening of breaches in the coastal barriers deals with flood hazard management and habitat conservation (Pye and Blott, 2009; Durand et al., 2010; Pollard et al., 2021). The threats to coastal communities due to the damage of property (including loss in life) have led to an in-depth assessment of the storm overwash induced breaching hazards on coastal barriers (Schoonees et al., 1998; Kraus et al., 2002; Plant et al., 2010; Plant and Stockdon, 2012; Stockdon et al., 2012, 2013; Plomaritis et al., 2018).

This present study deals with the assessment of the flooding risk of a low-lying inhabited area of the Laneros peninsula after the opening of a breach in the Sillon de Talbert spit barrier (North Brittany). This breach opened in March 2018 in the proximal section of the barrier spit (Suanez et al., 2018a), leading the inhabitants and politicians of the municipality to fear the possibility of coastal flooding. While the scientific council of the Sillon de Talbert Natural Reserve refused any engineering intervention (such as those proposed by Stéphan et al., 2018a) aimed at filling the breach with sediment replenishment, the mayor of Pleubian wished to carry out a study on the coastal flooding risk of the low-lying zone of the Laneros Peninsula located behind the breach. Besides the purely scientific aspects, the objective of this study was also to give the potentially impacted inhabitants accurate information on the potential flooding. This study was carried out between 2020 and 2021 with the help of a consulting company specializing in hydrodynamic modelling, taking into account several hypothetical scenarios of morphological evolution of the breach and/or the barrier in its proximal part.

2. Study area

2.1. Geomorphologic and hydrodynamic setting

The gravel barrier spit of the Sillon de Talbert is located on the northern coast of Brittany in the department of Côtes d'Armor (Fig. 1). This coast experiences a megatidal tidal range of up to ~11 m for the highest astronomical tide (SHOM, 2016). The most frequent swells come from the WNW with a resultant vector of around 303°N (Fig. 1b). Consequently, the waves break with an angle according to the average coastline's orientation (~50°N). Therefore, this non-parallel swash alignment generates a longshore current oriented from the SW to the NE. The most frequent offshore wave heights (H_{m0}) range between 1 and 1.5 m,

and between 9 and 10 s for wave period (T_p). During storms, wave heights can reach 9 m with periods of 20 s (Suanez et al., 2022).

The Sillon de Talbert gravel barrier spit stretches over 3.5 km long and it is composed of a volume reaching $1.23x10^6$ m^3 of sandy-gravel sediment (Stéphan et al., 2012). This barrier shelters a large intertidal zone corresponding to a sandflat scattered with reefs and some Pleistocene marine deposits. The highest parts of the sandflat are covered with a dense halophyte vegetation, particularly in the La Petite Grève area towards the back of the proximal part of the spit (Fig. 2b). The barrier spit is driven by both longshore and cross-shore dynamics (Stéphan et al., 2018a; Suanez et al., 2018a), however, since cross-shore sediment transfers are dominant as compared to longshore sediment transfers (430,000 m^3 *vs* 52,000 m^3 between 2002 and 2019) (Suanez et al., 2020), the Sillon de Talbert is considered to be a single-ridge swash-aligned barrier. According to the morphological and sedimentary features, Stéphan et al. (2012) have subdivided the barrier into four distinct morphosedimentary units (Fig. 1c), from the proximal sandy dune section (Unit 1) to the gravel distal section (Unit 4). These two sections are the most stable in terms of shoreline dynamics, while the last two sections, corresponding to the proximal gravel section (Unit 2) and the gravel median section (Unit 3), have displayed the largest retreat since 1930, up to –160 m and –150 m, respectively (Stéphan et al., 2012, 2018a; Suanez et al., 2018a). The long-term morphological evolution of the Sillon de Talbert indicates that at the beginning of the 18th century its morphology has changed from a barrier anchored at both ends, to a barrier spit disconnected from the islets of the Olone archipelago located in the NE (Fig. 1c) (Stéphan et al., 2012). This change of morphology increased the longshore sediment transport through a cannibalization process, mainly throughout the 19th and 20th centuries with the sediment depletion and rollover of the landward displacement of the barrier spit. As indicated above, Stéphan et al. (2012) calculated an average of landward migration rate of up to –1.1 $m.yr^{-1}$ between 1930 and 2010. More recently, Stéphan et al. (2018a) and Suanez et al. (2018a) indicated an increase of this averaged rate over the last fifteen years (2002-2017), reaching –2 $m.yr^{-1}$. A recent study based on a high frequency survey carried out along two beach profiles between 2012-2019 shows a landward migration rate reaching –3.3 to –4.3 $m.yr^{-1}$ (Suanez et al., 2022). Both longshore and cross-shore dynamics affecting sediment transport and spit barrier migration lead to the opening of a breach on March 2018 on the proximal section of the spit barrier (Suanez et al., 2018a).

2.2. Management policy and human settlement setting

The Sillon de Talbert is part of a protected natural area called "*Réserve Naturelle Régionale du Sillon de Talbert*" (https://www.reserves-naturelles.org/sillon-de-talbert) created in 2006 by the Brittany region and the French State. The perimeter of this nature reserve covers around 205 hectares (Fig. 2a). In addition, the "*Conservatoire du Littoral*" has established a preemption area on the privately owned lands bordering the southern limit of the nature reserve, which was extended to include the archipelago of Olone in 2018 (Fig. 2a). Three stakeholders have established a management plan for a period of five years: the Brittany region, Conservatoire du Littoral, and the local authorities (municipality of Pleubian). The latter is in charge of the implementation of the management actions, which are defined and voted on by the scientific council of the natural reserve. Therefore, the municipality of Pleubian, through the authority of the mayor, cannot carry out any intervention on the morphology of the Sillon de Talbert barrier spit –especially in terms of engineering works– without the agreement of the scientific council of the nature reserve.

The gravel spit barrier acts as a "natural structure" for coastal defense. It mainly protects the Laneros peninsula located behind the proximal section of the spit (Fig. 1). The role of coastal defense is even more important as this peninsula is urbanized (Fig. 2b). Though most of the housing is located in the south of the peninsula, there are still a few isolated houses close to the shoreline on the north coast. As indicated in the paragraph above (section 2.1.), the question of the risk of coastal flooding, even if very limited in this area, arose when the breach opened in March 2018 in the proximal section of spit.

Figure 2b illustrates the morphological and hydrodynamic context taking into account the Mean High Water Spring tide (MHWS) which reaches 4.83 m asl, and the Highest Astronomical Tide (HAT), which reaches 5.89 m asl (above sea level –asl– used throughout the text refers to the topographic reference level corresponding to the French geodetic Datum NGF-IGN69). We can see that on the north coast of the peninsula, about ten houses near the shoreline are potentially subject to the risk of coastal flooding. Indeed, the highest astronomical tide level (HAT) is very close to these houses, especially in the sector of La Petite Grève (Fig. 2c) and Mer Mélen (Fig. 2d), between the neighborhoods of Le Québo to the west, and Laneros to the east. This sector is low-lying and oriented from the north to the south, which extends to the very dense housing zone located to the south. It is mainly in this sector that the risk of coastal flooding is of the greatest concern for the local population.

3. Opening and morphological evolution of the breach

The opening of the breach in the proximal part of the Sillon de Talbert took place between the 3rd and 4th of March 2018, during a high spring tide (tide level decreased from 5.54 to 5.18 m asl between March 3rd and 4th, and surge from 0.39 to 0.34 m) and fair offshore wave conditions (significant wave height from 1.22 to 0.40 m) (Figs 3a and 3b). The breach opening was therefore due to the barrier flooding by a tide with strong ebb tide current, not by energetic waves. As indicated above, this rupture was part of a long process of erosion of the proximal part of the barrier through a cannibalization phenomenon (Suanez et al., 2018a). This evolution resulted in a very significant reduction in the width of the barrier in this weakened sector (Fig. 3c), which the authors described as a "wasp's waist" (Stéphan et al., 2018a).

The significant morphological evolution of the breach was extremely rapid and significant during the first year after it opened. The topo-morphological survey undertaken from February 2018 using KAP (Kite Aerial Photography) and UAVs (Unmanned Aerial Vehicle) indicated wide-spread morphological changes (Fig. 4a). Between February 2018 and May 2023, the breach gradually widened by about 50 m and deepened of about 3 to 3.5 m (Fig. 4b). The evolution of the coastline in the area of the breach shows that the retreat of the western bank has been continuous over time, following an east-west progression (Fig. 4c). The evolution of the eastern bank is more complicated. It has resulted in a lowering of the beach profile of up to 2.5 m due to the landward migration through a rollover process (Fig. 4b,c).

However, since the end of 2019 and beginning of 2020, the breach channel incision has stopped with the complete removal of the soft sedimentary accumulation of the barrier (sands and pebbles). Much of this sandy material actually built up a large flood lobe that accumulated as a washover fan in the back-barrier salt marsh, which grew over time (Fig. 5a,b,c). Beyond the morphosedimentary and hydrodynamic aspects, the accumulation of this sandy washover fan has also had an impact on the marsh's ecological environment, particularly in terms of flora. Since 2020, the erosive dynamics have impacted the compact and resistant Pleistocene hard clay layer, which significantly limits the incision of the channel through the breach (Fig. 5d). Currently, the current main evolution of the breach is a continuous retreat of its western bank, and a displacement by rollover of its eastern bank, which tends to flatten through a spreading of the material (Fig. 4b,c).

4. Data and methods

The numerical modelling system employed in the present study to further analyse the effect of the Sillon de Talbert gravel barrier breaching on the hydrodynamics of the area is described in this section, along with the required data and forcing processess.

4.1. Dataset

4.1.1. Topo-bathymetric data

The topo-bathymetric setting used in the modelling system corresponds to a merging from three different sources. The first dataset is a high resolution (1 x 1 m) topo-bathymetric digital elevation model (DEM) produced by IFREMER using airborne LiDAR measurements from October 2002 (Boersma and Hoenderkamp, 2003). These data cover both the terrestrial and the intertidal zone up to a depth of –5 m asl, from the Jaudy estuary in the west to the Bréhat archipelago in the east. The second dataset corresponds to the DEMs (ante- and post-breach opening, i.e. September 2017 and October 2019, respectively) produced as a part of the topo-morphological survey of the Sillon de Talbert (Stéphan et al., 2018b, 2023). These data were collected using DGPS measurements in *Real Time Kinematics* mode. The third dataset consists of the bathymetry, extended from the tidal zone to the shelf platform, corresponding to the DEM HOMONIM provided by the *Service Hydrographique et Océanographique de la Marine* (SHOM), with a resolution of ~100 m.

4.1.2. Tidal, wave and atmospheric forcing

The predicted astronomical tides were obtained from the tidal database FES 2014 (finite element solution), produced by Noveltis, Legos, and CLS and distributed by Aviso+, with support from Cnes (Carrere et al., 2016), using 34 harmonic tidal constituents with a spatial resolution of 1/16°.

Offshore wave data from 1994 to 2016 were obtained from the HOMERE hindcast dataset (Boudière et al. 2013). This hindcast was generated with the WAVEWATCH III® (WW3) spectral model (Roland and Ardhuin, 2014; Tolman and the WAVEWATCH III® Development Group, 2014). The model is based on an unstructured grid covering the Channel - Bay of Biscay area with a spatial resolution of ~250 m in the coastal zone. The model was forced by wind fields from the NCEP-CFSR (NOAA) reanalysis with a spatial resolution

ranging from 0.25° to 0.5° (Saha et al., 2010) and by the surface currents generated from an atlas of harmonic tidal constituents obtained from outputs of the MARS circulation model (Lazure and Dumas, 2008).

Wind (speed and direction) and atmospheric pressure fields were accounted for the hydrodynamic part of the numerical modelling system in order to represent storm surge, wind-induced currents, and their effects on wave fields. They were obtained from the CFSR (Climate Forecast System Reanalysis) database produced by the NCEP and based on a global model that uses observations from data sources including surface observations, upper air balloon observations, aircraft observations, and satellite observations (Saha et al., 2010).

4.2. Model description

The numerical modelling system uses the hydrodynamic model Telemac-2D (Ata, 2018), coupled with the phase-averaged wave model TOMAWAC (Fouquet, 2018).

4.2.1. Telemac-2D for hydrodynamic modelling

The Telemac-2D model, developed by the "Laboratoire National d'Hydraulique et Environnement" (LNHE), was used to simulate hydrodynamic conditions. Telemac-2D solves the shallow-water (Saint-Venant) hydrodynamic equations using finite-element or finite-volume methods on unstructured computational meshes. These equations express the conservation of mass (continuity equation) and the conservation of momentum (dynamic equations) in the two horizontal space directions (2DH) at any point of the computational domain. Telemac-2D has been frequently used to simulate hydrodynamic conditions in coastal, river, and estuarine zones (Breugem, 2020) as it deals with non-permanent free surface flows in shallow water. The model uses unstructured meshes, which are skilled in representing complex geometries by locally refining the resolution of the computational grid near the shoreline (Galland et al., 1991).

Telemac-2D takes into account the meteorological effects by integrating wind and atmospheric pressure, and calculates wave-induced currents, and wave setup based on the concept of radiation stress. The model can also simulate hydrodynamic conditions on the intertidal zones alternatively covered and uncovered by the water over time.

4.2.2. TOMAWAC for wave propagation

The TOMAWAC simulation module is used to model spectral wave progradation in coastal areas. It is based on the wave action density evolution equation (i.e. the energy density divided by the pulsation). Since TOMAWAC is a "third generation" model, it does not impose any parameterization on the spectral or directional distribution of the wave energy (or wave action). The simulation includes various processes such as *(i)* wave-bottom interaction (including refraction, shoaling, bottom friction, and breaking depth effects), *(ii)* wave-atmosphere interaction (including wind-to-wave energy transfer, white capping, nonlinear energy transfers between frequency quadruplets effects), *(iii)* wave-current interaction (including refraction, shoaling, counter-current breaking), and *(iv)* wave-tide interaction.

4.2.3. Wave-currents interactions

The interactions between currents and waves can lead to variations in the wave direction, frequency, and amplitude (Ardhuin et al., 2012; Villas Bôas et al., 2020). In the macro to megatidal environments, the effects of currents on waves are emphasised by the tide. The dissipation of waves by strong currents (wave blocking effect) is parameterized according to the formulation by Van der Westhuysen (2012). When wave propagation is impeded by an opposing current, wave height and steepness increase and can break. An energy transfer within the wave spectrum can then be observed in areas with strong currents. These effects are simulated by coupling Telemac-2D and TOMAWAC data every 1 minute, in order to provide information to each other, i.e., water depth and current from Telemac-2D to TOMAWAC and radiation stresses from TOMAWAC to Telemac-2D.

4.2.4. Model domain and boundary conditions

The employed numerical modelling system is based on a finite element method (FEM) using a unique unstructured grid (triangular meshes) for both hydrodynamic and wave modules. Unlike regular grids, the meshes associated with unstructured grids can be coarse in a wide zone far from the study area, becoming finer the closer you get to the area of interest. In this study, a single grid was used consisting of 56,175 nodes and 110,642 triangular elements. In order to correctly represent large-scale hydrodynamic processes such as tide propagation, the computational grid extends over ~108 km along the west-east direction, from the Primel Cap (Plougasnou town) to the Fréhel Cap, and extends up to 35 km offshore to the

north of the Sillon de Talbert (Fig. 6a). The offshore limit of the computational grid has been defined in such a way that the positions of the 2D sea-state spectra (frequency/direction) in the HOMERE database (yellow circles in Fig. 6a) approximatively correspond approximately with nodes of the grid boundary. Offshore, the coarser mesh resolution is about 2-3 kilometres (see G1 in Fig. 6a). The resolution of the mesh progressively decreases from 500 m to 200 m between Île-Grande and Minard Cap (see G2 in Fig. 6b), then from 100 m between the Trieux and the Jaudy Rivers (see G3 in Fig. 6c) to ~50 m in front of the Sillon de Talbert (from Crec'h Maout Cap to Laneros Peninsula) (Fig. 6c), and from 5 m to 2 m in the tidal zone and the breach, respectively (see G4 in Fig. 6d).

The model used tidal elevation forcing data from the FES 2014 tidal database and hourly wave spectra from the WW3 HOMERE database (see section 4.1.2.). Output locations bordering the offshore boundary of the model domain were used to force the TOMAWAC model by interpolating the wave spectra along the offshore nodes of the model boundary. For the nodes forming the terrestrial boundary of the model, a "free evolution of the flow" condition was specified. In addition, CFSR atmospheric data (wind and pressure, see section 4.1.2.) were been considered for the wind-driven currents, the storm surge, and the wind-driven wave generation modelling.

Several tests were conducted and focused on the bottom friction law (Strickler, roughness length, etc.) and the associated friction coefficient. This parameterization was carried out mainly on water levels, and to a lesser extent on currents (not shown). The optimal parameterization deduced from this step led to the use of Strickler's Law with a coefficient of 25 for the friction on the bottom, and the Smagorinsky parameterization for the turbulence.

4.3. Hydrodynamic validation

4.3.1. Water level validation

Validation of the water level produced by Telemac-2D was completed by the comparison to the predicted tide levels calculated by the SHOM at three different locations (i.e. Port Béni in the west, Les Héaux-de-Bréhat to the north, and Bréhat Men Joliguet in the east) (see Fig. 6b), and for three tide conditions (i.e., mean high water neap - MHWN, mean high water spring - MHWS, and highest astronomic tide - HAT). SHOM reference data used here are neither measurements nor numerical model outputs, but result from a tidal harmonic analysis carried out over available *in-situ* measurements, followed by a recomposition on

MHWN, MHWS, HAT tide conditions (SHOM, 2005). Estimated from *in-situ* measurements during MHWS condition, the mean (normalized) errors on harmonic tidal prediction provided in SHOM (2005) is less than 15% for the maximum current velocities, and less than 30 minutes for the average phase lag. In the three reference ports of Port Béni, Les Héaux-de-Bréhat, and Bréhat Men Joliguet (see Fig. 6b), the validation of water level also based on tidal harmonic analysis indicates the RMSE is between 10-12 cm, i.e. about 1% of the total water level. These predictions and associated errors are derived from few days of *in-situ* observations (respectively 181, 132, and 72 days at Bréhat Men Joliguet, Les Héaux-de-Bréhat, and Port Béni). These values are in line with those given in previous studies (Giloy et al., 2023).

The validation of Telemac-2D outputs showed that the amplitude and phase of the tide were accurately reproduced for the three tide conditions with R^2 of 0.99 and RMSE increasing from 0.04 m to 0.14 m from MHWN condition to HAT condition, respectively (Fig. 7a,b,c). These margins of error are negligible in comparison with the tidal range (around 1-2%).

4.3.2. Tidal current validation

Validation of the current velocity and orientation obtained by the Telemac-2D model was also carried out by comparing the model results with the predictions made by the SHOM (2005) at four different locations in the studied area (Fig. 6a). These data correspond to the hourly values of current velocity and orientation associated with the MHWN and MHWS conditions. The comparison we conducted showed that the Telemac-2D model is less consistent, with R^2 (ranging from 0.68 to 0.95) and RMSE tending to increase, the closer we get to the coast. Thus, at point #1, the largest error margins are between 0.18 and 0.25 $m.s^{-1}$; and they decrease significantly at point #4 to reach 0.07 and 0.12 $m.s^{-1}$ (Fig. 7d,e). However, the maximum of velocity magnitudes in both directions are close to those from the SHOM model. The slight phase shift is mainly due to the differences in the temporal resolution of tide predictions, hourly and every 15 minutes for the SHOM model and Telemac-2D model, respectively. Differences could also be attributable to the different bathymetric data, bottom friction, or resolution used by the SHOM model and that of our study, especially in the shallow zone. Despite these uncertainties, the Telemac-2D model reproduces current directions and velocities satisfactorily.

4.3.3. Wave validation

Validation of the WW3 HOMERE dataset was carried out using records from a pressure sensor OSSI 010-003C (Ocean Sensor Systems Inc.®, 1.5 cm accuracy) installed in the intertidal zone at coordinates 48°52'34.4554 "N; -3°4'58.9127", and at a depth of –0.461 m asl depth (see Fig. 6c) (Suanez et al., 2018b). Correlation between both *in-situ* and WW3-simulated wave heights (H_{m0}) was achieved over the period 2012-2016, using a dataset extracted at the point #65423 (i.e., model node from WW3 HOMERE database) located at 48°52'36" N; -3°4'52 "W, and at a depth of –0.56 m asl (see Fig. 7f). The choice of this extraction point was conditioned by the fact that it was the closest of the OSSI pressure sensor location. The results show a good agreement between the two datasets, with R^2 of 0.77 and RMSE of 0.24 m, despite a slight global overestimation of H_{m0} (WW3) compared with *in-situ* H_{m0} (OSSI) as shown by Q-Q plot graph (Fig. 7g). Comparison of the two datasets also shows an underestimation of the highest WW3-simulated wave height. It is a systematic bias of the WW3 model, which has difficulty in reproducing the most extreme events (Mureau et al., 2022). The biases observed between the two series for extreme values are also related to *in-situ* recordings, as the pressure sensor is installed in the intertidal zone. Thus, when the depth of the water column is at a minimum while the tide is rising or falling, aberrant water level values are recorded. Therefore, all recordings at +1h and -1h before or after the sensor is submerged are removed as they are considered outliers. When the correlation is restricted to wave records associated with tide levels above MHWS (i.e., 4.83 m asl) and HAT (i.e., 5.89 m asl), the fits are significantly improved, with R^2 increasing from 0.86 to 0.93, respectively, and an RMSE of 0.29 m (Fig. 7h,i).

4.4. Modelling strategy

The approach followed in this study was to model an extreme hydrodynamic event likely to generate significant coastal flooding. The associated simulations were based on five topo-morphological configurations for the gravel spit. Three of them correspond to hypothetic scenarios for the future morphological evolution of spit.

4.4.1. Extreme event selection

The choice of the most significant hydrodynamic event to model was based on the morphological and hydrodynamic monitoring of the Sillon de Talbert over the last two

decades. Based on the analysis of the morphological changes extracted from annual DEMs measurements, and the hydrodynamic conditions (wave and water level) over the period 2002-2017, Suanez et al. (2018a) identified 11 significant morphogenetic events combining extreme wave height and water levels. Wave height was thresholded using the 2% exceedance offshore wave height of 3.15 m, and the highest water level using the 2% exceedance water level of 5.5 m (Tab. 1).

As shown in Table 1, storm Anne on February 1-2, 2014 was the most energetic event recorded over these 15 years of survey data. This high-energy storm exhibited a long wave period (T_p) of up to 18.2 seconds combined with high H_{sig} values up to 4.2 m. This event led to major morphological changes, as the maximum landward migration of the spit barrier reached between –30 to –20 m. These observations were confirmed by the study of morphological changes carried out using higher-frequency monitoring, based on monthly measurements of beach profiles (Suanez et al., 2022). For this study, covering the period 2012-2019, the analysis of morphological changes was also complemented by a study of the hydrodynamic conditions (wave and water level), which showed that the February 1, 2014 event generated the highest catastrophic overwash of the barrier spit with a water flow exceeding the crest by between 0.8 and 0.5 m.

For modelling, the observed tide levels recorded for this event were increased by around 80 to 90 cm at the model boundaries. This additional height makes it possible to reach the extreme water levels for a 100-year return period (i.e. between 6.4 and 6.6 m NGF) that have been statistically calculated by SHOM for the Sillon de Talbert area (SHOM/CETMEF, 2012). These centennial water levels are used to consider the exceptional nature of an extreme event, which constitutes the reference level in the methodological approach recommended by the French government for mapping the risk of marine flooding (Azzam et al., 2014).

4.5. Five morphological configurations for modelling

Hydrodynamic conditions (water level including tide, surge, and wave setup, and associated currents) were modelled taking into account five topo-morphological configurations (Fig. 8). Configurations #1 and #2 correspond to the ante-breach and post-breach morphological settings. They consist of the DEMs of 1 x 1 m resolution from

September 2017 (i.e. 6 months before the barrier breaching; see Fig. 8a) and October 2019 (i.e. 18 months after the barrier breaching; see Fig. 8b), respectively. As indicated previously (i.e. section 4.1.1.), these data come from DEM measurements of the entire barrier spit carried out as part of the annual survey of morphological changes of the Sillon de Talbert (Stéphan et al., 2018b; 2023). Configurations #3, #4, and #5, are based on prospective scenarios. They take into account a barrier spit morphology based on the DEM of October 2019, which was deliberately modified.

Configuration #3 (Fig. 8c) illustrates a moderate breaching scenario, with the breach widening up to 300 m and a deepening up to 2.7 m asl over the next few years (~2025). The widening of the breach in this scenario was achieved by *(i)* eroding the western bank of the breach (value corresponding to this erosion was calculated by linear regression from measurements taken between March 2018 and December 2019), and *(ii)* by lowering the crest of the eastern bank of the breach of up to 4.20 m asl (below the MHWS tide level of 4.83 m asl) over a length of 300 m. This prospective scenario was also based on measurements taken during March 2018 to December 2019 (see Fig. 4c). The 2.7 m elevation of the deepening of the breach channel corresponds to the Pleistocene clay forming a hard non-erodible layer (see Fig. 5d). Finally, this configuration also took into account the nearly 10 m landward migration of the eastern bank of the breach, after the evolution of this section between March 2018 and December 2019 (see Fig. 4c).

Configuration #4 (Fig. 8d) illustrates the widening breaching scenario up to of 500 m. The same prospective approach as the configuration # 3 was used for the erosion of the western bank. For the eastern bank, we just considered the lowering of up to 4.83 m (corresponding to the MHWS tide level) of this section over a longer distance, as being the consequence of the medium term (i.e. 5 to 10 years) landward displacement of the barrier in the context of sediment depletion.

Finally, configuration #5 (crest lowering scenario) illustrates a complete lowering of the barrier after a complete removal of the crest due to catastrophic overwash events (Fig. 8e). The DEM constructed to simulate hydrodynamic conditions under this fictitious configuration corresponds to a modified version of the DEM from October 2019. The crest elevation was defined at 4.83 m asl because it corresponds to both the MHWS tide level and the lowest post-storm elevation measured along the barrier crest over the period 2002-2020. In this configuration, we also assumed a cross-shore sediment transfer from the crest to the back-barrier area, leading to a retreat by rollover and a widening of the crest. The volume of this cross-shore sediment was taken into account to estimate the corresponding retreat values of

the barrier. Volumetric calculations were performed along 70 cross-sections using Surfer 10 software®. The retreat of the barrier (r) was then estimated using the following formulation:

$$r = \frac{V}{L*H} \quad [2]$$

where *V* is the volume of sediment above the MHWS tide level, *L* is the length of the section, and *H* is the difference between the elevation of the back-barrier area and the MHWS tide level.

5. Results

5.1. High spring tide water levels and currents

Water levels and tidal current velocities associated with a tidal coefficient of 115 (i.e., near HAT condition) were first simulated for topo-morphological configurations #1 and #2, corresponding to the ante-breaching DEM of September 2017, and the post-breaching DEM of September 2019, respectively, without considering wave and atmospheric (wind and pressure) forcings (Fig. 9). At this stage, only tide effects were simulated in real conditions, without including the water level increase of around 80 to 90 cm corresponding to a 100-year event. The simulated water levels clearly show differences between the NW ocean side and the SE back-barrier sandflat. One hour before high tide (HT-1h), the water level simulated on the ocean-side is only a few centimeters higher than on the back-barrier side (~5cm), inducing tidal currents flowing north-eastwards along the spit until they reach the tip where the velocity increases as the water penetrates into the sandflat area (Fig. 10a). This tidal circulation pattern is observed under configurations #1 and #2. However, in configuration #2, southward tidal currents are flowing through the breach channel with a maximum velocity of 0.75 $m.s^{-1}$ (Fig. 10b,c).

During high tide (HT), the water level simulated on the back-barrier side appears ~25 cm higher than on the ocean side (Fig. 9) while ebb tide currents (oriented north to north-west) increase in flow velocity at the tip of the gravel spit (Fig. 10d). The circulation pattern of the tidal currents is similar for configurations #1 and #2. However, in configuration #2, the difference in water level on either side of the barrier induces strong outflow tidal currents through the breach, where flow velocities reach about 2.2 $m.s^{-1}$ (Fig. 10e,f).

One hour after high tide (HT+1h), water levels are higher, up to 37 cm in the back-barrier area (Fig. 9). In this case, the highest tidal current velocities are located at the tip of the spit for configuration #1 (Fig. 10g). For configuration #2, strong outflow tidal currents are flowing through the breach channel, again with velocities of 2.2 $m.s^{-1}$ (Fig. 10h,i).

5.2. Extreme event simulations of 1rst February 2014 storm

5.2.1. Post-breach situation: configuration #2

For configuration #2, the significant wave heights simulated at high tide reach 2.9 m at 500 m offshore the gravel barrier (Fig. 11a). Wave heights decrease to about 2.2 m as they propagate to the beach face due to wave energy dissipation on the reef platform. In the back-barrier area, simulated wave heights along the shoreline are less than 0.5 m from Le Québo in the west to Laneros in the east (Fig. 11b). The simulations show no significant increase in wave height in the back-barrier zone, leading to negligible wave setup (< 0.02 m) (Fig. 11b).

One hour before high tide (HT-1h), the simulated currents through the breach are oriented southwards (onshore) and reach a velocity of 1.8 $m.s^{-1}$ (Fig. 12a). At high tide (HT) and at the beginning of the ebb tide (HT+1h), the currents are oriented offshore through the breach before flowing north-eastward along the spit at about 1 $m.s^{-1}$ (Fig. 12b,c).

5.2.2. 300 m length breach enlargement: configuration#3

For configuration #3, the H_{sig} and wave setup simulated at high tide on the back-barrier side reach 1 m and 0.08 m, respectively. The highest simulated H_s values in this area are located in front of the locality of Run Traou (Fig. 11b). Despite the enhanced wave height in the back-barrier area between configurations #2 and #3 due to the enlargement of the breach, simulated HT water levels are 5 cm lower in configuration #3 (Fig. 13a). In this case, the lower water level is linked to an increased draining of the sandflat area through a larger section of the breach. Similarly, the reduction in flood and ebb tide current velocities between configuration #3 and configuration #2 can be explained by the enlargement of the breach (Fig. 12).

5.2.3. 500 m long breach enlargement: configuration #4

The simulation for configuration #4 are quite similar to those for configuration #3. The significant wave height and wave setup along the back-barrier are less than 1 m and 0.1 m, respectively. The highest simulated H_s values are located along the inhabited coastline of Mer Melen (Fig. 11b). The current circulation pattern is also close to that observed in configuration #3. Simulated HT water levels in the back-barrier are 0.025 to 0.05 m lower than for configuration #2, also due to increased draining of the sandflat (Fig. 13b).

5.2.4. Crest lowering situation: configuration #5

Despite the complete overwash of the barrier, the simulated wave heights for configuration #5 do not exceed 0.8 m above the crest before decreasing on the back-barrier area, except in front of the Pen Vir promontory, where H_s values reach about 1 m (Fig. 11b). Wave setup never exceeds 0.1 m along the back-barrier area shoreline (Fig. 11a). Similarly to the results obtained for configurations #3 and #4, the simulated HT water levels are about 0.05 m lower than for configuration #2 (Fig. 13c).

The simulated currents show two main differences compared with configuration #2. Firstly, the HT currents are oriented onshore despite the difference in water levels on either side of the barrier (Fig. 12k). These currents are no longer linked to the tide, but to the predominance of waves overwashing the complete barrier. Secondly, the decrease of the flood and ebb current velocities is linked to a lower difference in water level on either side of the barrier when completely flooded.

6. Discussion

6.1. Uncertainties in the modelling approach

The model simulations were based on the extreme storm event of 1 February, 2014, which is considered to be the most morphogenic event that has impacted the Sillon de Talbert over the last 20 years (Suanez et al., 2018a; 2022). The severe morphological impacts of this storm were also reported in other coastal zones of Brittany, where topo-morphological monitoring has been carried out for several years, or even decades (Blaise et al., 2015; Stéphan et al., 2018b, 2019, 2022; Suanez et al., 2023). The realistic hydrodynamic conditions for this event were numerically reproduced except for the tide level, which was increased in

order to correspond to a 100-year return period water level. In this sense, the methodological approach adopted is in line with government recommendations, which state that the most extreme event should be taken into account when assessing the risk of coastal flooding (Perherin et al., 2012; Azzam et al., 2014). However, as indicated by Pirazzoli (2000) when analysing datasets from three tide gauges located on the west and north coasts of Brittany, "the highest sea surges [due to storm events] of the last decades did not occur at the time of spring high tide". Therefore, this approach introduces a degree of uncertainty given by the fact that when we compare the wave characteristics at the peak of the storm at the time of high tide, i.e., February 1, 2014 at 7:00 pm, the simulations at the pressure sensor location indicate that H_{m0} and T_{moy} are ~2.7 m and ~10.9 s, for a centennial water depth of ~6.5 m. In comparison, *in-situ* recordings from the OSSI pressure sensor indicate a wave height and period of ~2.1 m and ~10.9 s, for a "real" water depth of ~5.8 m. The artificially increased water level at the model boundary contributes to explain these higher modeled H_{m0} values compared with *in-situ* measurements ($H_{sig\text{-}OSSI}$), but it still goes in the direction of a conservative modelling strategy regarding flooding risk.

Uncertainties in the modelling approach depend on a number of different factors including the model inputs, the accuracy of the model calibration, the boundary conditions, the bathymetric grid resolution, the forcing data, and the simulated physical processes. As indicated above, if the validation of the model simulations showed good agreement between the simulated and measured tide water levels with high correlations (R^2 >0.99) and low errors (*RMSE* between 0.04 to 0.16 m), the errors between the simulated and measured tide currents were larger, with *RMSE* ranging from 0.07 to 0.25 $m.s^{-1}$ (see Fig. 7). The mentioned above, the slight phase shift is due to differences in temporal resolution between the two SHOM data sets and the Telemac-2D simulations. As it is often the case with hydrodynamic modelling, the accuracy of the bathymetric data, which affects the reliability of simulated physical processes such as currents or bottom friction, particularly in the shallow water zone, is also a determining factor (Jacob and Stanev, 2021; Alday et al., 2022; Umgiesser et al., 2022).

The input wave conditions are obtained from WW3 simulations at grid points located at different water depths along the open boundary of the model (see Fig. 6a), without any knowledge of the errors between the *in-situ* wave height and the simulated wave height at these locations. However, the estimated *RMSE* and bias from Boudière et al. (2013) were 0.13 and 0.05 m, respectively, measured at the Pierres Noires wave buoy (situated off the west coast of Brittany) located at a depth of ~60 m. More recently, a study assessing the scales of spatial representativeness of the sea state parameters recorded by 11 buoys along the French

Atlantic coastline (including a buoy located north of the study site) was carried out using retrospective simulations from the WW3 wave model hindcast (Mureau et al., 2022). The statistical errors (*RMSE* and bias) for wave height (H_s) computed between the model and *in-situ* data at each buoy location reach average of 0.25 m and 0.08 m respectively, up to 0.37 m and 0.27-0.33 m for both buoys located off the Brittany coast. The authors attribute this coastal sea state variability to several environmental factors, such as the presence of islands, shoals and rugged coastline, the amplified tidal currents and sea level variations over the shelf, and the intermediate to shallow water conditions together with the strong bathymetric gradients. The role of these environmental factors, in particular the complexity of the bathymetry of the platform, in altering the accuracy of numerical simulations is also highlighted by Dissanayake et al. (2021). As indicated by the authors, even if the unstructured grid allows to increase the spatial resolution from the offshore to the shallow zone, the bathymetric variations may not be always represented accurately.

Modelling uncertainties depend also on the topo-morphological configurations used in the different simulation scenarios that put into consideration the high mobility of the barrier of the Sillon de Talbert in time and space. As shown by Matias et al. (2012), based on wave flume experiments (Barrier Dynamics Experiment: BARDEX), the sensitivity of barriers to flooding depends essentially on wave conditions, sedimentological characteristics (including porosity, permeability and sediment size) and the morphological state of the barrier before the storm. Therefore, during a single overwash event, gravel barriers experiment successively crestal building, lowering and/or complete removal, which, through feedback, induce a change in hydrodynamic conditions (Matias et al., 2014). However, these studies are still highly experimental, and do not provide general statements on the hydro-morphosedimentary functioning that can be extrapolated to all barriers. In any case, these elements have not been taken into account in the modelling carried out as part of this study. In this paper, three configurations have considered a continuation of the erosive evolution trends measured in recent years, from the widening of the breach (configurations #3 and #4) to the complete levelling of the barrier (configuration #5). These topo-morphological configurations can have great uncertainties when considering the expected climate changes (including meteorological conditions) in the coming years. Hartley and Pontee (2008) distinguish two categories of uncertainties inherent in predicting future coastal evolution: *(i)* epistemic uncertainties, which relate to a lack of appropriate data or knowledge, and *(ii)* random uncertainties, which relate to stochastic behaviour of coastal barriers leading to the formation and evolution of breaches. One of the greatest uncertainties associated with breaching processes is the rate of expansion

of breaches once formed, which depends on the combination of forcing factors and existing beach states. Given this, the simulations presented in this paper should only be considered only as a tool for reflection and decision-making for coastal management in terms of flooding hazard.

Also, the use of a phase-averaged model in the present study did not allow us to investigate the potential effect of infragravity (IG) waves (Bertin et al., 2018) and swash dynamics at the back-barrier shoreline in the context of a breach enlargement. While the conservative approach employed in the present study (i.e., increasing by ~1 m the water level at the open boundary for the extreme event simulations, leading to an offshore high tide level up to ~70 cm higher than the HAT level) should mostly compensate for the lack of IG waves in the model (in terms of their potential effect on high water levels reached in the back-barrier area at the IG time scale), applying a phase-resolving model to this very specific site, or at least a model accounting for the dynamics of IG waves (such as XBeach model in 'surf beat' mode), would surely be a relevant perspective for future work. In the meantime, it is worth noting that choosing the most extreme event in terms of wave forcing will not necessarily induce the highest flooding risk in all circumstances, as for instance shown by Bertin et al. (2014). That is partly why, in the present study, the selection of an extreme event is combined with the fact of significantly increasing the water level at the open boundary to reach a conservative enough modelling strategy. It has been also shown that ‘extreme’ washover deposits can be mostly related to the presence of large IG waves but not necessarily to large storm surges (Baumann et al., 2017), which adds to the discussion about selecting an extreme event.

Finally, it should be pointed out that the methodological approach used in this study does not take into account the impact of climate change on future sea-level rise. As previously mentioned, the reference water level used in this study was indeed defined on the basis of an extreme tide water level for a 100-year return period + wave setup (centennial water level: CWL), in line with government recommendations for assessing the risk of submersion (Azzam et al., 2014). However, these recommendations indicate that the centennial water level should be raised by 0.2 m to take account of sea-level rise in 10 to 20 years' time. The short-term hazard is therefore calculated as $RSL_{10\text{-}20yrs}$ = CWL + 0.2 m. Secondly, it is also recommended to take into account the future sea level rise for the year 2100, by raising the centennial level by 0.6 cm. The 100-year reference water level is thus calculated as follows = RSL_{2100} = CWL + 0.6 m. The value of 0.6 m corresponds to the projections formulated by the IPCC in its 5th report of 2013, indicating, for the worst-case scenario, a rise in sea level of

between 0.45 and 0.82 m, with an average value of 0.62 m (IPCC, 2013). Thus, using this approach for our study area, $RSL_{10\text{-}20yrs}$ equals 6.80 m asl and RSL_{2100} equals 7.2 m asl. As can be seen, these reference water levels are well above the extreme water levels simulated for the February 1, 2014 event, which do not exceed 6.38 ± 0.14 m asl on the back of the Sillon de Talbert barrier, particularly on the breach area. In any case, these reference water levels must now be reviewed, as the sixth IPCC report has revised the future rise in sea level upwards for the year 2100, giving an average value of around +1.30 m for the worst-case scenario RCE8.5 (Openheimer et al., 2019; IPCC, 2023).

6.2. Impact on flood hazards along the inhabited back-barrier shoreline

The model simulations clearly show that the Sillon de Talbert forms a physical boundary separating two water bodies (i.e. the ocean-side *vs* the back-barrier) characterized by specific tidal dynamics, with a time lag of about 15 minutes in the tidal peak and a difference of about 25 cm in high tide level. The difference in tide water levels on either side of the barrier becomes more pronounced at the beginning of the ebb tide and can reach 30 cm during spring tides. This tidal characteristic is specific to the south-west coast of the English Channel, where the main semi-diurnal tidal component (M2) propagates from west to east with an increasing tidal range that is locally accentuated due to resonance phenomena (linked to the M4 tidal component) in response to the morphological configuration of the shoreface/foreshore zone (Pingree and Maddock, 1978). This specific phenomenon occurs in our study area, where a broad, gently sloping platform extends over a ~10 km offshore distance, from the shoreline to –10 m asl depth. Propagating eastwards, the tidal wave bypasses the tip of spit (including the reefs of the Olone archipelago), and progresses into the back-barrier zone where it is locally amplified due to the shallow water. Therefore, in the back-barrier sandflat, the tidal peak occurs 15 minutes later and the high tide water level is higher than on the ocean-side zone. As a result, ebb currents begin to flow before the high tide level is reached. The asymmetry between the ebb and flood currents is significant at the tip of the spit, where the high flow velocities have accumulated a large ebb gravel lobe in N-NW direction (Fig. 1c).

This tidal pattern is quite specific to the Sillon de Talbert, considering that for most of coastal barrier systems, back-barrier areas are affected by low amplitude tide-induced water level fluctuations due to limited hydrological connectivity between the ocean-side and the lagoon-side (Kraus, 2003; Kraus et al., 2008; Austin et al., 2013). However, barrier breaching

enhances the water exchanges between the ocean-side and the back-barrier areas, which, in turn, may modify the hydrodynamics functioning of the tidal inlets. Velasquez-Montoya et al. (2018) recently simulated the effects of sea-level rise, and subsequent tidal inlet morphodynamics, due to the surge of hurricane Sandy (October 29, 2012) on the lagoon-side at the Pea Island barrier-system (North Carolina) breaching. They showed that the rise of water level rise at the lagoon-side also increased the water level gradients between the ocean-side and the lagoon-side and strengthened the ebb currents in the tidal inlet.

The simulations carried out in the ante- and post-breach configurations (configurations #1 and #2, respectively) indicate that the Sillon de Talbert breaching currently has no significant impact in terms of tide water level condition changes (Fig. 9). However, in hypothetical configurations #3 to #5, the breach widening and/or the barrier crest lowering induces a decrease in the water level gradient on either side of the gravel barrier and reduces the high tide water levels (including wave setup) by a few centimetres (up to 5 cm) on the back-barrier zone. By draining part of the tidal prism, the breach acts as a communicating vessel, particularly in the back-barrier salt marsh where discharge currents directed offshore are simulated at high tide. The survey of morphological changes of the breach area undertaken from March 2018 also confirms the predominant role of ebb currents in the sediment transfers through the breach (Fig. 4). Most of the sediment eroded in the breach section was transferred northwards to the lower beach face of the spit, then remobilized by the waves. Therefore, while a flood delta has accumulated on the back-barrier salt marsh since the breach opening (see section 3), it concerns a small volume of sediment when compared to the volume of ebb current sediment transfer.

The modelling indicates that widening the breach (i.e. configurations #3 and #4) tends to reduce the risk of coastal flooding in the low-lying areas of the Lanéros peninsula by decreasing the water levels reached at high tide in the back-barrier area. Importantly, the lowering of high tide water level largely counterbalances the wave setup induced by wave propagation in the back-barrier zone through the breach. Thus, the total water level (i.e. tide + wave setup) simulated on the back-barrier for configurations #3 to #5 remains lower than (or almost equal to) the water level reached in the current topo-morphological configuration #2. These results therefore show that the breach has no significant effect on the coastal flooding hazards in the short term. It seems unlikely that this situation will change significantly in the next few years.

6.3. Impact on erosion hazards along the inhabited back-barrier shoreline

Hydrodynamic simulations showed that during extreme event conditions, the storm wave propagation *(i)* through the breach channel and/or *(ii)* overtop the inundated section of the barrier, is relatively limited despite breach widening or crest lowering considerations in future scenarios. For configurations #3 to #5, simulated wave heights reach a maximum height of ~1 m along a limited section of the back-barrier shoreline during the energy peak of storm event. This value decreases by 25% to 50% one hour before and after high tide. Therefore, we can assume that barrier breaching should not lead to significantly more energetic hydrodynamic conditions and increased erosion hazards along the inhabited coastline in the coming years. The morphodynamic of this back-barrier zone is expected to be more controlled by local wind-generated waves, rather than energetic offshore storm waves, which remain occasional as indicated by Suanez et al. (2018a, 2022).

While the configuration #5, which considers a very low barrier profile, including a crest of 60 to 90 m wide and lowered to the MHST level, remains the worst case hypothetical scenario, it is based on the topo-morphological measurements taken after several intense morphogenic events inducing significant catastrophic overwash (Stéphan et al., 2010; Suanez et al., 2022). Therefore, this scenario might be representative of the future (decades to centuries) significant morphological changes of the Sillon de Talbert considering the long-term retreat of the spit over the last decades (Stéphan et al., 2012) and centuries (Pinot et al., 1994). This configuration allows us to assess whether the barrier still plays a significant role in storm wave attenuation for such a simulation. Simulations for configuration #5 show that even if the barrier crest is completely inundated at high tide, the barrier "body" still plays a major role in wave attenuation. However, the wave height at the crest, up to a maximum of 0.80 m, is still high, given that extreme water levels ε of 0.45 m lead to sluicing-to-catastrophic overwash regimes responsible for significant landward displacements of the spit by rollover (Suanez et al., 2022). This element needs to be taken into account in the coastal management strategy, as the catastrophic flooding of single-ridge barriers (such as the Sillon de Talbert) is often a source of concern for local residents and/or elected representatives, particularly when the back-barrier zones are urbanized. In such cases, managed realignment measures or nature-based soft management solutions can be vigorously challenged. As mentioned by Hudson and Baily (2018) in the case of Porlock beach in UK, monitoring of overwash events then appears as essential in understanding geomorphological evolution, but also to reassure the public and inform coastal managers in relation to the long-term stability of the barrier features.

6.4. A new strategy in terms of coastal risk management

As mentioned above, the refusal of the scientific council of the Sillon de Talbert nature reserve to artificially fill the breach through an engineering operation contrasts radically with the coastline management policies that have been implemented for decades on this site (Pinot, 1994; de Beaulieu, 2000; Stéphan et al., 2012).

In 1969, the management of the Sillon de Talbert, which was then a private domain of the State, was transferred to an inter-municipal syndicate to which the commune of Pleubian belonged (*syndicat mixte intercommunal pour la sauvegarde et la protection du sillon de Talbert*). From the early 1970s, the management strategy aimed to fix the shoreline in order to prevent the chronic retreat of the spit. Between 1974 and 1975, over 1,100 m of frontal rip-rap and a groin were installed on the proximal section, in the Chouck beach area (Fig. 3a). In 1982, the frontal rip-rap was extended to the median section, reaching 1,400 m, while some lowered sections of the spit were reprofiled using bulldozers until 1987 (de Beaulieu, 2000). In 1988, the local authorities even attempted to enclose the pebbles in fishing nets which were quickly destroyed by storms. For most cases, these expensive interventions (up to 1,000,000 euros in 1988, corresponding to ~2,000,000 euros in 2024) were carried out hastily, without any prior scientific study to support them.

Faced with these failures, the choice of a new nature-based management strategy was made by the Nature Reserve's newly created scientific council in the early 2000s (Houron, 2018). Most of the riprap was removed and scientific monitoring of the morphological evolution of the spit was undertaken (Stéphan et al., 2012). Thus, when the breach was opened in 2018, the choice of scientific expertise (such as that of the present study) was preferred to an engineering intervention.

The solution currently being considered for naturally filling the breach is to remove the last riprap (i.e. the Chouk groin and the two frontal riprap on either side) (see Fig. 3a). In this way, the retreat of the shoreline would deliver sediment to the longshore drift, which could naturally fill the breach (Stéphan et al., 2018a). However, this solution presupposes that the last private homes on the seafront are bought out and demolished by the *Conservatoire du Littoral*. At present, houses #3, #4 and #5 have been purchased (see Fig. 3a), and house #3 will be demolished by the end of 2024. Houses #1 and #2 have yet to be acquired by the *Conservatoire*, but they are still not for sale.

7. Conclusion

This modelling study has showns that the recent opening of the breach, which impacted the Sillon de Talbert spit barrier, has no significant or immediate consequences in terms of flooding risk in the low-lying urbanized area at the back-barrier. The results obtained for different topo-morphological configurations underline the fact that hydrodynamic changes in the area behind the barrier show no significant rise in maximal water levels, while the very flat topography of the salt marsh results in a significant decrease in wave energy conditions propagating through the breach (i.e. even for worst-case scenarios involving widening of the breach or severe erosion of the coastal barrier). This study, commissioned by local authorities and coastal managers, was instrumental in reassuring the local population living in the low-lying areas of the Laneros peninsula. It also supports the new coastal management strategy adopted almost two decades ago by the Nature Reserve and the *Conservatoire du Littoral*. In western France, the management of coastal erosion very often still leads to the use of hard defence structures, making the Sillon de Talbert spit one of the few coastal sites where a sustainable and adaptive management approach has been implemented. By removing the hard defence structures along the spit in 2002, coastal managers adopted an erosion management approach based on natural dynamics. However, in the coming decades (looking ahead to the 2100s), this nature-based solution will need to be complemented by a more ambitious spatial planning strategy, particularly for built-up areas, to face future sea-level rise and mitigate the risk of marine flooding in low-lying areas at the back-barrier.

Acknowledgements

The simulations were carried out using parallelized calculations on the HPC (High Performance Computing) supercomputer DATARMOR of the "*Pôle de Calcul et de Données pour la Mer – PCDM* " of IFREMER (https://wwz.ifremer.fr/pcdm). Monitoring of the Sillon de Talbert is carried out as part of the "*Service d'Observation National*" SNO-DYNALIT (https://www.dynalit.fr/), and is financially supported by the French "*Institut National des Sciences de l'Univers – INSU*", the French coastal research infrastructure (IR-ILICO), and the French "*Ministère de l'Enseignement Supérieur, de la Recherche, et de l'Innovation*". The surveys are also benefited from the Labex-Mer (ANR-10-LABX-0019) program between 2011 and 2018, and by the ISblue program, the Interdisciplinary graduate school for the blue planet (ANR-17-EURE-0015), since 2019. Both of these programs were co-funded by a grant

from the French government under the program "*Investissements d'Avenir*" embedded in France 2030. This work was also supported by the municipality of Pleubian and the Conservatoire du Littoral.

References

Alday, M., Ardhuin, F., Dodet, G., Accensi, M. 2022. Accuracy of numerical wave model results: application to the Atlantic coasts of Europe, *Ocean Science*, 18 (6), 1665–1689. https://doi.org/10.5194/os-18-1665-2022.

Almeida, L.P., Masselink, G., Russell, P.E., Davidson M.A., 2015. Observations of gravel beach dynamics during high energy wave conditions using a laser scanner. Geomorphology, 228, 15–27. https://doi.org/10.1016/j.geomorph.2014.08.019.

Ardhuin, F., Roland, A., Dumas, F., Bennis, A.-C., Sentchev, A., Forget, P., Wolf, J., Girard, F., Osuna, P., Benoit M. 2012. Numerical wave modelling in conditions with strong currents: dissipation, refraction, and relative wind. Journal of Physical Oceanography, 42, 2101–2120. https://doi.org/10.1175/JPO-D-11-0220.1.

Ata, R. 2018. TELEMAC-2D V8p0 User Manual, 130 p. http://www.opentelemac.org/.

Austin, M.J., Masselink, G., McCall, R.T., Poate, T.G. 2013. Groundwater dynamics in coastal gravel barriers backed by freshwater lagoons and the potential for saline intrusion: Two cases from the UK. Journal of Marine Systems, 123–124, 19–32. https://doi.org/10.1016/j.jmarsys.2013.04.004.

Azzam, C., Sabine Baillarguet, S., Bouet, A., Brodhag, E., Desire, Kavaj, A. Perherin C., Renaud, A. (Eds.). 2014. Guide méthodologique : Plan de prévention des risques littoraux. Ministère de l'Écologie, du Développement durable, et de l'Energie (MEDDE), Paris, 169 p.

Barnard, P., Hoover, D., Hubbard, D., Snyder, A., Ludka, B.C., Allan, J., Kaminsky, G.M., Ruggiero, P., Gallien, T.W., Gabel, L., McCandless, D., Weiner, H.M., Cohn, N., Anderson, D.L., Serafin, K.A. (2017). Extreme oceanographic forcing and coastal response due to the

2015–2016 El Niño. Nature Communications, 8, 14365. https://doi.org/10.1038/ncomms14365

Baumann J., Chaumillon E., Bertin X., Schneider J.-L., Guillot B., Schmutz M. 2017. Importance of infragravity waves for the generation of washover deposits. Marine Geology, 391, 20-35. https://doi.org/10.1016/j.margeo.2017.07.013.

Bertin, X., Li, K., Roland, A., Zhang, Y.J., Breilh, J.F., Chaumillon, E. 2014. A modeling-based analysis of the flooding associated with Xynthia, central Bay of Biscay. Coastal Engineering,
94, 80-89. https://doi.org/10.1016/j.coastaleng.2014.08.013.

Bertin, X., de Bakker, A., van Dongeren, A., Coco, G., Andrée, G., Ardhuinf, F., Bonneton, P., Bouchette, F., Castelle, B., Crawford, W., Davidson, M. , Deen, M., Dodet, G., Guérin, T., Inch, K., Leckler, F., McCall, R., Muller, H., Olabarrieta, M., Roelvink, D., Ruessink, G., Sous, D., Stutzmann, E., Tissier, M. 2018. Infragravity waves: From driving mechanisms to impacts. Earth-Science Reviews, 177, 774-799. https://doi.org/10.1016/j.earscirev.2018.01.002.

Billson, O, Russell, P, Davidson, M. 2019. Storm waves at the shoreline: When and where are infragravity waves important? Journal of Marine Science and Engineering, 7(5), 139. https://doi.org/10.3390/jmse7050139

Blaise, E., Suanez, S., Stephan, P., Fichaut, B., David, L., Cuq, V., Autret, R., Houron, J., Rouan, M., Floc'h, F., Ardhuin, F., Cancouët, R., Davidson, R., Costa, S., Delacourt, C. 2015. Bilan des tempêtes de l'hiver 2013-2014 sur la dynamique de recul du trait de côte en Bretagne. *Géomorphologie: relief, Processus, Environnement*, 21 (3), 267–294. https://doi.org/10.4000/geomorphologie.11104

Boersma, S.M., Hoenderkamp, K., 2003. Tregor, Final Report IFREMER. (Amsterdam).

Boudière, E., Maisondieu, C., Ardhuin, F., Accensi, M., Pineau-Guillou, L., Jérémy, L.J., 2013. A suitable metocean hindcast database for the design of marine energy converters.

International Journal of Marine Energy, 3–4, e40–e52. https://doi.org/10.1016/j.ijome.2013.11.010

Breugem, W.A., 2020. Ongoing developments in TELEMAC and TOMAWAC at IMDC. In: Breugem, W.A., Frederickx, L., Koutrouveli, T., Chu, K., Kulkarni, R., Decrop, B. (Eds.), Online proceedings of the papers submitted to the 2020 TELEMAC-MASCARET User Conference, October 2020 (Antwerp), International Marine & Dredging Consultants (IMDC), S. 115–121.

Buscombe, D., Masselink, G., 2006. Concepts in gravel beach dynamics. Earth-Science Reviews, 70 (1-2), 33–52. https://10.1016/j.earscirev.2006.06.003.

Carrere, L., Lyard, F., Cancet, M., Guillot, A., Picot, N., 2016. FES 2014, a new tidal model - Validation results and perspectives for improvements. In: Proceedings of the ESA living planet symposium, (Prague, 9-13 May 2016)**,** 9–13.

Carter, R.W.G., Orford, J.D., 1981. Overwash processes along a gravel beach. Earth Surf. Process. Landf., 6 (5), 413–426. https://doi.org/10.1002/esp.3290060503.

Carter, R.W.G., Orford, J.D., 1984. Coarse clastic barrier beaches: A discussion of the distinctive dynamic and morphosedimentary characteristics. Mar. Geol., 60 (1–4), 377–389. https://doi.org/10.1016/0025-3227(84)90158-0.

de Beaulieu, F. 2000. Le sillon de Talbert. Armen, 112, 2–9.

Dissanayake, P., Yates, M.L., Suanez, S., Floc'h, F., Krämer, K. 2021. Climate change impacts on coastal wave dynamics at Vougot Beach, France. Journal of Marine Science and Engineering, 9 (9), 1009. https://doi.org/10.3390/jmse9091009.

Dornbusch, U., 2017. Design requirement for mixed sand and gravel beach defences under scenarios of sea level rise. Coast. Eng., 124, 12–24. https://doi.org/10.1016/j.coastaleng.2017.03.006.

Durand, P., Anselme, B., Thomas, Y.-F., 2010. L'impact de l'ouverture de la brèche dans la langue de Barbarie à Saint-Louis du Sénégal en 2003 : un changement de nature de l'aléa inondation ? Cybergeo, 496. https://doi.org/10.4000/cybergeo.23017.

Elsayed, S.M., Oumeraci, H., 2016. Combined modelling of coastal barrier breaching and induced flood propagation using XBeach. Hydrology, 3 (4), 32. https://doi.org/10.3390/hydrology3040032.

Elsayed, S.M., Oumeraci, H., 2018. Modelling and mitigation of storm-induced saltwater intrusion: Improvement of the resilience of coastal aquifers against marine floods by subsurface drainage. Environmental Modelling & Software, 100, 252–277. https://doi.org/10.1016/j.envsoft.2017.11.030.

Forbes, D.L., Orford, J.D., Carter, R.W.G., Shaw, J., Jennings, S.C., 1995. Morphodynamic evolution, selforganisation, and instability of coarse-clastic barriers on paraglacial coast. Mar. Geol., 126 (1-4), 63–85. https://doi.org/10.1016/0025-3227(95)00066-8.

Fouquet, T., 2018. TOMAWAC V8p0r3 User Manual, TELEMAC-MASCARET System Software 2018.

Galland, J.C., Goutal, N., Hervouet, J.M., 1991. TELEMAC: A new numerical model for solving shallow water equations. Advances in water resources, 14 (3), 138–148. https://doi.org/10.1016/0309-1708(91)90006-A.

Giloy, N., Latapy, A., André, G. 2023. Estimation of skew surge uncertainties when predicting tides in the past. Weather and Climate Extremes, 41, 100597. https://doi.org/10.1016/j.wace.2023.100597.

Hartley, L., Pontee, N., 2008. Assessing breaching risk in coastal gravel barriers. Proceedings of the Institution of Civil Engineers-maritime Engineering, 161 (4), 143–152. https://doi.org/10.1680/maen.2008.161.4.143.

Houron J., 2018. Le sillon de Talbert (Pleubian, Côtes d'Armor) : Réserve Naturelle Régionale. Bulletin de la Société Géologique et Minéralogique de Bretagne, 16 (série d), 55–63.

Hudson, C., Baily, B., 2018. Delivering sustainable coasts: Monitoring the long-term stability of a breached barrier beach, Porlock Bay, Somerset, United Kingdom. Ocean & Coastal Management, 152, 88–99. https://doi.org/10.1016/j.ocecoaman.2017.11.022.

IPCC, 2013. Climate Change 2013: The Physical Science Basis. Contribution of Working Group I to the Fifth Assessment Report of the Intergovernmental Panel on Climate Change. In: Stocker, T.F., D. Qin, G.-K. Plattner, M. Tignor, S.K. Allen, J. Boschung, A. Nauels, Y. Xia, V. Bex and P.M. Midgley (eds.), Cambridge University Press, Cambridge, United Kingdom and New York, NY, USA, 1535 p.

IPCC, 2023. Climate Change 2023: Synthesis Report. Contribution of Working Groups I, II and III to the Sixth Assessment Report of the Intergovernmental Panel on Climate Change. In: Core Writing Team, Lee, H., Romero, J. (Eds.), IPCC, Geneva, Switzerland, p. 35-115, https://doi.org/10.59327/IPCC/AR6-9789291691647.

Jacob, B., Stanev, E.V., 2021. Understanding the impact of bathymetric changes in the German Bight on coastal hydrodynamics: one step toward realistic morphodynamic modeling. Front. Mar. Sci., 8 (640214), https://doi.org/10.3389/fmars.2021.640214.

Jennings, R., Shulmeister, J., 2002. A field based classification scheme for gravel beaches. Mar. Geol., 186 (3–4), 211–228. https://doi.org/10.1016/S0025-3227(02)00314-6.

Kraus, N.C., Militello, A., Todoroff, G., 2002. Barrier breaching processes and barrier spit breach, Stone Lagoon, California. Shore & Beach, 70 (4), 21–28.

Kraus, N.C., Wamsley, T.V., 2003. Coastal barrier breaching, Part 1: Overview of breaching processes. Coastal and Hydraulics Engineering Technical Note ERDC/CHL CHETN-IV-56, US Army Corps of Engineers, Engineer Research and Development Center, Coastal and Hydraulics Laboratory, Vicksburg, MS, 14p. https://erdc-library.erdc.dren.mil/jspui/bitstream/11681/1964/1/CHETN-IV-56.pdf

Kraus N.C., Patsch K., Munger S., 2008. Barrier beach breaching from the lagoon side, with reference to Northern California. Shore & Beach, 76 (2), 33–43.

Lazure, P., Dumas, F., 2008. An external–internal mode coupling for a 3D hydrodynamical model for applications at regional scale (MARS). Advances in Water Resources, 31 (2), 233–250. https://doi.org/10.1016/j.advwatres.2007.06.010.

Leatherman, S.P., 1979a. Migration of Assateague Island, Maryland, by inlet and overwash processes. Geology, 7 (2), 104–107. https://doi.org/10.1130/0091-7613(1979)7<104:MOAIMB>2.0.CO;2.

Leatherman, S.P. (Eds.), 1979b. Barrier Islands from the Gulf of St. Lawrence to the Gulf of Mexico. Academic Press, New York, 325 p.

Li, X., Leonardi, N., Plater, A.J., 2020. Impact of barrier breaching on wetland ecosystems under the influence of storm surge, sea-level rise and freshwater discharge. Water, 40, 771–785. https://doi.org/10.1007/s13157-019-01219-x.

Matias, A., Williams, J.J., Masselink, G., Ferreira, Ó., 2012. Overwash threshold for gravel barriers. Coastal Engineering, 63, 48-61. https://doi.org/10.1016/j.coastaleng.2011.12.006.

Matias, A., Blenkinsopp, C.E., Masselink, G., 2014. Detailed investigation of overwash on a gravel barrier. Marine Geology, 350, 27-38. https://doi.org/10.1016/j.margeo.2014.01.009

Mureau, G., Dodet, G., Suanez, S., 2022. Characterizing sea state variability along the French Atlantic coast. In Levacher, D., Benoit, M., Sanchez M., Teles M. (Eds.): Actes du colloque des XVIIème Journées Nationales Génie Civil – Génie Côtier, Chatou, 11-13 Octobre 2022, 129–142. https://doi.org/10.5150/jngcgc.2022.015.

Nienhuis, J.H., Heijkers, L.G.H., Ruessink, G., 2021. Barrier breaching versus overwash deposition: Predicting the morphologic impact of storms on coastal barriers. Journal of Geophysical Research: Earth Surface, 126 (6), e2021JF006066. https://doi.org/10.1029/2021JF006066.

Oppenheimer, M., Glavovic, B.C., Hinkel, J., van de Wal, R., Magnan, A.K., Abd-Elgawad, A., Cai, R., Cifuentes-Jara, M., DeConto, R.M., Ghosh, T., Hay, J., Isla, F., Marzeion, B., Meyssignac, B., Sebesvari, Z., 2019. Sea Level Rise and Implications for Low-Lying Islands, Coasts and Communities. In: Pörtner, H.-O., Roberts, D.C., Masson-Delmotte, V., Zhai, P., Tignor, M., Poloczanska, E., Mintenbeck, K., Alegría, A., Nicolai, M., Okem, A., Petzold, J., Rama, B., Weyer, N.M. (Eds.), IPCC Special Report on the Ocean and Cryosphere in a Changing Climate, Cambridge University Press, Cambridge, UK and New York, NY, USA, p. 321–445. https://doi.org/10.1017/9781009157964.006.

Orford, J.D., Carter, R.W.G., 1982. Crestal overtop and washover sedimentation on a fringing sandy gravel barrier coast, Carnsore Point, Southeast Ireland. Journal of Sedimentary Research, 52 (1), 265–278. https://doi.org/10.1306/212F7F2C-2B24-11D7-8648000102C1865D.

Orford, J.D., Carter, R.W.G., Forbes, D.L., 1991. Gravel barrier migration and sea level rise: some observations from Story Head, Nova Scotia, Canada. Journal of Coastal Research, 7 (2): 477–488. https://www.jstor.org/stable/4297854.

Orford, J.D., Carter, R.W.G. Jennings, S.C., Hinton, A.C., 1995. Processes and timescales by which a coastal gravel-dominated barrier responds geomorphologically to sea-level rise: Story head barrier, Nova Scotia. Earth Surf. Process. Landf., 20 (1), 21–37. https://doi.org/10.1002/esp.3290200104.

Orford, J.D., Carter, R.W.G., 1995. Examination of mesoscale forcing of a swash-aligned, gravel barrier from Nova Scotia. Mar. Geol., 126 (1–4), 201–211. https://doi.org/10.1016/0025-3227(95)00078-D.

Orford, J.D., Carter, R.W.G., Jennings, S.C., 1996. Control domains and morphological phases in gravel-dominated coastal barriers of Nova Scotia. J. Coast. Res., 12 (3), 51–85. https://www.jstor.org/stable/4298507.

Orford, J.D., Forbes, D.L., Jennings, S.C., 2002. Organisational controls, typologies and time scales of paraglacial gravel-dominated coastal systems. Geomorphology, 48 (1–3), 51–85. https://doi.org/10.1016/S0169-555X(02)00175-7

Orford, J.D., Anthony, E.J., 2011. Extreme events and the morphodynamics of gravel-dominated coastal barriers: strengthening uncertain ground. Mar. Geol., 290 (1–4), 41–45. https://doi.org/10.1016/j.margeo.2011.10.005.

Perherin, C., Azzam, C., Kergadallan, X., 2012. Révision du guide méthodologique plans de prévention des risques littoraux : une meilleure prise en compte de l'ensemble des phénomènes pour la connaissance de l'aléa submersion marine. Actes des 34èmes journées de l'hydraulique (SHF, Paris, 1-2 février 2012). https://www.persee.fr/doc/jhydr_0000-0001_2012_act_34_1_1239.

Pingree, R.D., Maddock, L., 1978. The M4 tide in the English Channel derived from a non-linear numerical model of the M2 tide. Deep Sea Research, 25 (1), 53–63. https://doi.org/10.1016/S0146-6291(21)00006-0.

Pinot, J-P., 1994. Fixer le plan ou gérer le profil : l'exemple du Sillon du Talberv. Cahiers Nantais, 41–42, 307–316.

Pirazzoli, P.A., 2000. Surges, atmospheric pressure and wind change and flooding probability on the Atlantic coast of France. Oceanologica Acta, 23 (6), 643–661. https://doi.org/10.1016/S0399-1784(00)00122-5.

Plant, N.G., Stockdon, H.F., Sallenger, A.H., Turco, M.J., East, J.W., Taylor, A.A., Shaffer, W.A., 2010. Forecasting hurricane impact on coastal topography. Eos Trans. AGU, 91 (7), 65–66. https://doi.org/10.1029/2010EO070001.

Plant, N.G., Stockdon, H.F., 2012. Probabilistic prediction of barrier-island response to hurricanes. Journal of Geophysical Research Earth Surface, 117 (F03015). https://doi.org/10.1029/2011JF002326.

Plomaritis, T.A., Ferreira, O., Costas, S., 2018. Regional assessment of storm related overwash and breaching hazards on coastal barriers. Coast. Eng., 134, 124–133. https://doi.org/10.1016/j.coastaleng.2017.09.003.

Poate, T., Masselink, G., McCall, R., Russell, P., Davidson, M., Turner, I.L., 2013. High frequency in-situ field measurements of gravel beach response during storm conditions. Mar. Geol., 342, 1–13. https://doi.org/10.1016/j.margeo.2013.05.009.

Pollard, J.A., Christie, E.K., Brooks, S.M., Spencer, T., 2021. Impact of management regime and regime change on gravel barrier response to a major storm surge. J. Mar. Sci. Eng., 9 (2), 147. https://doi.org/10.3390/jmse9020147.

Pye, K., Blott, S.J., 2009. Progressive breakdown of a gravel-dominated coastal barrier, Dunwich–Walberswick, Suffolk, U.K.: processes and implications. J. Coast. Res., 25 (3), 589–602. https://www.jstor.org/stable/27698354

Roland, A., Ardhuin, F., 2014. On the developments of spectral wave models: Numerics and parameterizations for the coastal ocean. Ocean Dynamics, 64 (6), 833–846. ttps://doi.org/10.1007/s10236-014-0711-z.

Saha, S., Moorthi, S., Pan, H.-L., Wu, X., Wang, J., Nadiga, S., Tripp, P., Kistler, R., Woollen, J., Behringer, D., Liu, H., Stokes, D., Grumbine, R., Gayno, G., Wang, J., Hou, Y.T., Chuang, H.Y., Juang, H.M.H., Sela, J., Iredell, M., Treadon, R., Kleist, D., van Delst, P., Keyser, D., Derber, J., Ek, M., Meng, J., Wei, H., Yang, R., Lord, S., van den Dool, H., Kumar, A., Wang, W., Long, C., Chelliah, M., Xue, Y., Huang, B., Schemm, J.K., Ebisuzaki, W., Lin, R., Xie, P., Chen, M., Zhou, S., Higgins, W., Zou, C.Z., Liu, Q., Chen, Y., Han, Y., Cucurull, L., Reynolds, R.W., Rutledge, G., Goldberg, M., 2010. The NCEP Climate Forecast System reanalysis. Bulletin of the American Meteorological Society, 91 (8), 1015–1057. https://doi.org/10.1175/2010BAMS3001.1.

Schoonees, J.S., Lenhoff, L., Raw, A.J., 1998. Preventing natural breaching of the major sand spit protecting the port of Walvis Bay. Coastal Engineering Proceedings, 1 (26), 1475–1488. https://doi.org/10.1061/9780784404119.109.

SHOM, 2005. Courants de marée des côtes de France (Manche/Atlantique). Produit numérique. https://diffusion.shom.fr/marees/courants-de-maree/courants-2d.html

SHOM, 2008. LITTO3D®. https://services.data.shom.fr:/geonetwork/srv/api/records/BATHYMETRIE_L3D.xml.

SHOM/CETMEF (2012). Statistiques des niveaux marins extrêmes des côtes de France (Manche et Atlantique). ISBN 978-2-11-128331-2.

Stéphan, P., Suanez, S., Fichaut, B., 2010. Franchissement et recul des cordons de galets par rollover. Impact de la tempête du 10 mars 2008 dans l'évolution récente du Sillon de Talbert (Côtes d'Armor, Bretagne). Norois, 215, 59–75. https://doi.org/10.400/norois.3252.

Stéphan, P., Suanez, S., Fichaut, B., 2012. Long-term morphodynamic evolution of the Sillon de Talbert gravel barrier (Brittany, France). Shore Beach, 80 (1), 19–36.

Stéphan, P., Suanez, S., Fichaut, B., Autret, R., Blaise, E., Houron, J., Ammann, J., Grandjean, P., 2018a. Monitoring the medium-term retreat of a gravel spit barrier and management strategies, Sillon de Talbert (North Brittany, France). Ocean Coast. Manag. 158, 64–82. https://doi.org/10.1016/j.ocecoaman.2018.03.030.

Stéphan, P., Blaise, E., Suanez, S., Fichaut, B., Autret, R., Floc'h, F., Cuq, V., Le Dantec, N., Ammann, J., David, L., Jaud, M., Delacourt, C., 2019. Long to medium to short-term shoreline dynamics of the Brittany coast (Western France). Journal of Coastal Research, 88(SI), 89–109. https://doi.org/10.2112/SI88-008.1

Stéphan P., Suanez S., Houron J., Ammann J., Fichaut B., 2018b. Suivi pluri-décennal de la flèche de galets du Sillon de Talbert (Pleubian, Côtes d'Armor) à partir de modèles numériques de terrain (MNT). INDIGEO. https://doi.org/10.35110/8e37c01f-4cec-4edb-8c01-7047725f7dc4.

Stéphan P., Suanez S., Ammann J., Houron J., 2023. Données de suivi topo-morphologique de la brèche du Sillon de Talbert (Pleubian, Bretagne nord) par photogrammétrie (SfM). INDIGEO. https://doi.org/10.35110/ef77c22c-840a-48c2-b603-ad1d3167679b.

Stockdon, H.F., Sallenger, A.H., Holman, R.A., Howd, P.A., 2007. A simple model for the spatially-variable coastal response to hurricanes. Mar. Geol., 238 (1–4), 1–20. https://doi.org/10.1016/j.margeo.2006.11.004

Stockdon, H.F., Doran, K.J., Thompson, D.M., Sopkin, K.L., Plant, N.G., 2013. National Assessment of Hurricane-Induced Coastal Erosion Hazards : Southeast Atlantic Coast, U.S. Geological Survey Open-File Report 2013-1130. https://pubs.usgs.gov/of/2013/1130/pdf/ofr2013-1130.pdf.

Stockdon, H.F., Doran, K.J., Thompson, D.M., Sopkin, K.L., Plant, N.G., Sallenger, A.H., 2012. National Assessment of Hurricane-Induced Coastal Erosion Hazards : Gulf of Mexico, U.S. Geological Survey Open-File Report 2012-1084. https://doi.org/10.3133/ofr20121084.

Suanez, S., Stéphan, P., Floc'h, F., Autret, R., Fichaut, B., Blaise, E., Houron, J., Ammann, J., Grandjean, P., Accensi, M., André, G., Ardhuin, F., 2018a. Fifteen years of hydrodynamic forcing and morphological changes leading to breaching of a gravel spit, Sillon de Talbert (Brittany). Géomorphol. Relief Process. Environ. 24 (4), 403–428. https://doi.org/10.4000/geomorphologie.12677.

Suanez, S., Stéphan, P., Floc’h, F., 2018b. Mesures des conditions hydrodynamiques côtières le long du Sillon de Talbert (Pleubian, Bretagne nord). INDIGEO [dataset]. https://doi.org/10.35110/f6f2440a-4703-4352-8f3e-3f3999472b3c.

Suanez, S., Stéphan, P., Fichaut, B., Ammann, J., Accensi, M., 2020. Medium-Term Longshore and Cross-shore Dynamics of a Gravel Spit Driving by Storm Events (Sillon de Talbert, Brittany, France). J. Coast. Res., 95 (SI), 669–673. https://doi.org/10.2112/SI95-130.1

Suanez, S., Stéphan, P., Autret, R., Houron, J., Floc’h, F., David, L., Ammann, J., Accensi, M., André, G., Le Guyader, D., Cancouët, R., 2022. Catastrophic overwash and rapid retreat of the gravel spit barrier during storm events (Sillon de Talbert, North Brittany, France). Earth Surf. Process. Landf., 47 (8), 2014–2043. https://doi.org/10.1002/esp.5361.

Suanez, S., Yates, M.L., Floc'h, F., Accensi, M., 2023. Using 17 years of beach/dune profile monitoring to characterize morphological dynamics related to significant extreme water level events in North Brittany (France). Geomorphology, 433, 108709. https://doi.org/10.1016/j.geomorph.2023.108709.

Tolman, H.L. & the WAVEWATCH III® Development Group., 2014. User Manual and System Documentation of WAVEWATCH III® version 4.18. Technical Note 316. NOAA/NWS/NCEP/MMAB.

Tucker, M.J., Pitt, E.G., 2001. Waves in Ocean Engineering. Elsevier Science Ltd, 548p.

Umgiesser, G., Ferrarin, C., Bajo, M., Bellafiore, D., Cucco, A., De Pascalis, F., Ghezzo, M., McKiver, W., Arpaia, L. 2022. Hydrodynamic modelling in marginal and coastal seas - The case of the Adriatic Sea as a permanent laboratory for numerical approach. *Ocean Modelling*, 179 (102123). https://doi.org/10.1016/j.ocemod.2022.102123

van der Westhuysen, A.J., van Dongeren, A.R., Groeneweg, J., van Vledder, G.P., Peters, H., Gautier, C., van Nieuwkoop, J.C.C., 2012. Improvements in spectral wave modeling in tidal inlet seas. Journal of Geophysical Research, 117, C00J28, https://doi.org/10.1029/2011JC007837.

Velasquez Montoya, L., Sciaudone, E.J. Mitasova, H., Overton, M.F., 2018. Observation and modeling of the evolution of an ephemeral storm-induced inlet: Pea Island Breach, North Carolina, USA. Continental Shelf Research, 156, 55–69. https://doi.org/10.1016/j.csr.2018.02.002.

Villas Bôas, A.B., Cornuelle, B.D., Mazloff, M.R., Gille, S.T., Ardhuin, F., 2020. Wave–Current Interactions at Meso- and Submesoscales: Insights from Idealized Numerical Simulations. Journal of Physical Oceanography, 50, 3483–3500, https://doi.org/10.1175/JPO-D-20-0151.1.

Wamsley, V., Kraus, N.C., 2005. Coastal barrier island breaching, Part 2: Mechanical breaching and breach closure. Coastal and Hydraulics Engineering Technical Note

ERDC/CHL CHETN-IV-65, U.S. Army Corps of Engineers Washington, DC 20314-1000, 21p. https://apps.dtic.mil/sti/pdfs/ADA438882.pdf

Figure captions

Fig. 1. Location map. (a) regional scale; (b) local scale. Wave rose established from the data obtained by the ANEMOC numerical model over the period of 1979-2002 (source: *Laboratoire National d'Hydrolique et d'Environnement, LNHE-EDF Chatou, and CEREMA-Brest*) at the calculation point 3°12.66' W; 48°56.28' N; depth of 36.1 m. (c) Different longshore morphological units of the spit and representative beach profiles of the four units (after Suanez et al., 2018, modified).

Fig. 2. Anthropogenic features. (a) Protected areas of the "*Conservatoire du Littoral*" (yellow) and nature reserve (red). (b) Map of human settlements in habitats along the Laneros Peninsula coastline. Source: DEM is a merge of the 2012 LiDAR data from the *Service Hydrographique et Océanographique de la Marine* database Litto3D® (SHOM, 2008) and a drone measurement of the breach section achieved in 2019. Cadastral data on building locations for the entire study area come from the French government's open access database (https://cadastre.data.gouv.fr/). (c) and (d) Aerial photos of *La Petite Grève* (photo credit: J. Ammann 2023-03-02). (d) Aerial photography of *La Petite Grève* and Mer Melen-Laneros, respectively (photo credit: J. Ammann, 2023-03-02).

Fig. 3. (a) Aerial photo of the Sillon de Talbert before the opening of the breach (Photo credit: D. Halleux, September 23, 2009). (b) Aerial photo of the breach on the proximal section of the Sillon de Talbert 6 months after the opening (Photo credit: J. Ammann, September 14, 2018). Both photos show coastal defense structures and longshore currents. Numbers correspond to the houses built on the coastline. (c) Shoreline changes of the proximal section between 2002 and 2018. The limit of the shoreline is defined by the highest astronomical tide level (HAT) extracted from DEMs produced from 2002 to 2018.

Fig. 4. Morphological evolution of the breach based on elevation changes between September 2017 and December 2021 (a). (b) Morphological changes of the breach along the cross-shore profile A-B. (c) Shoreline changes on the breach area since it opened (from 07/03/2018 to 15/12/2021).

Fig. 5. Morphological changes of the breach zone between 2018 and 2023. a) Morphology of the breach six months after opening. No washover fan has yet accumulated (Photo credit: Jérôme Ammann – 13/09/2018). b) Washover fan corresponding to the sandy flood lobe accumulated on the back-barrier salt marsh through the breach of the Sillon the Talbert (Photo credit: Jérôme Ammann – 18/09/2019). c) Five years after the opening of the breach, the enlargement of the washover fan is linked to the widening of the breach, which favors more intense sediment transport (Photo credit: Jérôme Ammann – 02/03/2023). d) Photo taken on July 14, 2023 showing of the hard clay layer on the bottom of the breach (Photo credit: Julien Houron).

Fig. 6. Model setup based on a single unstructured grid, from coarse (G1: 2-3 km), to medium (G2: 500-200 m, and G3: 100-50 m), to small (G4: 5-2 m) spatial resolution. The yellow circles in (a) indicate the location of the HOMERE wave data extraction points used for wave forcing at the grid boundary. White crosses in (a) represent the location of the four calculation points used for the validation of the current velocity and direction between the Telemac-2D model and the predictions achieved by the SHOM. Yellow stars in (b) correspond to the three locations of tide predictions by the SHOM to validate the Telemac-2D simulated water levels. Yellow and green triangles (c) correspond respectively to wave measurement and modelling (WW3 HOMERE) points used in section 4.5.

Fig. 7. Comparison of water levels (m asl) between the Telemac-2D model (curves in blue) and the SHOM predictions (curves in red), for three tide conditions: (a) mean high water neap (MHWN) corresponding to the French tide coefficient 45, (b) mean high water spring (MHWS) corresponding to the French tide coefficient 95, and (c) high astronomical tide (HAT) corresponding to the French tide coefficient 115, for the three reference ports of Port Béni, Les Héaux-de-Bréhat, and Bréhat Men Joliguet (see Fig. 6b). Comparison of tidal currents (in $m.s^{-1}$) between the Telemac-2D model (curves in blue) and the SHOM tidal current predictions (curves in red) for a mean high water neap (d) and mean high water spring (d) at four different location extraction points (see Fig. 6a). Comparison of situ pressure

sensor (OSSI) and WW3-simulated (HOMERE) wave heights (H_{m0}) over the period 2012-2016 (f). Q-Q graph of the entire wave dataset (g). Comparison of both wave datasets for tide levels above MHWS (h) and HAT (i).

Fig. 8 – Five morphological configurations used for the hydrodynamic modelling (a-e). (f) Elevation cross-shore and longshore profils.

Fig. 9 − Simulated spring-high water levels around the Sillon de Talbert at three different times of high tide for configuration#1 and configuration#2. Water levels values are given for the three points A, B and C (white dots) located offshore, and on both sides of the breach, respectively. Maps on the left, centre and right show simulated water levels one hour before the high tide (HT-1h), at high tide (HT) and one hour after the high tide (HT+1h), respectively.

Fig. 10 − Simulated tidal currents around the Sillon de Talbert at three different times of high tide for configuration#1 and configuration#2. (a), (b), and (c) show simulated tidal currents one hour before the high tide (HT-1h). (d), (e), and (f) represent simulated tidal currents at high tide (HT). (g), (h), and (i) show simulated tidal currents one hour after the high tide (HT+1h).

Fig. 11 – Simulated significant wave height distribution and wave setup elevation at high tide for configurations #2 to #5 (a). Graphs in (b) represent the simulated wave height (left) and wave setup (right) extracted along a longshore transect located in the back-barrier area between points A and B. See (a) for the location of longshore transect.

Fig. 12 − Simulated currents at three different times of high tide for configuration#1 to #5. (a), (d), (g), and (i) show simulated currents one hour before the high tide (HT-1h). (b), (e), (h), and (k) represent simulated currents at high tide (HT). (c), (f), (i), and (l) show simulated currents one hour after the high tide (HT+1h).

Fig. 13 – Simulated water levels (WL) on the back of the Sillon de Talbert barrier for configurations #2 to #5 (see point C on Fig 9 for location of the simulation point). Histograms represent water level differences between configurations #2 and #3 (a), #2 and #4 (b), #2 and #5 (c).

Tab. 1 – Inventory of the major morphogenetic events combining extreme storm wave heights and water levels (after Suanez et al., 2018a, modified). The shaded line correspond to the simulated storm event of February 1, 2014 (storm Anne). The wave energy flux is calculated using the formulation (*F*) according to Barnard et al. (2017) as follow:

$$F = \frac{\rho g^2}{64\pi} H_{m0}^2 T \quad [1]$$

where *F* is expressed per unit crest length of the wave (in $J.m^{-1}s^{-1}$), ρ = 1,025 $kg.m^{-3}$ is the density of seawater, and g = 9.81 $m.s^{-2}$ is the gravitational acceleration, H_{m0} is the significant wave height, and *T* is the wave period.

Date	Storm name	H_{sig} (m)	Wave dir.	T_p (s)	Water level (m asl)	time	Wave energy ($J.m^{-1}s^{-1}$)
28/02/2002	*	3.2	300°	13.5	5.63	6:00 AM	6.784×10^7
20/03/2007	*	3.4	344°	7.6	5.56	6:00 AM	4.273×10^7
10/03/2008	Johanna	3.4	296°	13.7	5.95	7:00 AM	7.578×10^7
31/03/2010	*	3.8	302°	11.2	5.7	6:00 AM	7.898×10^7
01/02/2014	Anne	3.3	295°	12.3	5.98	6:00 AM	6.471×10^7
01/02/2014	Anne	4.2	298°	18.2	5.66	19:00 PM	15.750×10^7
02/02/2014	Anne	3.4	297°	16.7	5.89	7:00 AM	9.329×10^7
09/02/2016	Ruzica/Imogen	3.3	296°	16.4	5.54	6:00 AM	8.687×10^7
09/03/2016	*	3.2	302°	9.3	5.54	6:00 AM	4.620×10^7
03/01/2018	Eleanor	4.6	303°	13.1	5.61	6:00 AM	13.530×10^7
04/01/2018	Eleanor	3.4	300°	14.7	5.58	7:00 AM	8.344×10^7

Declaration of interests

☐The authors declare that they have no known competing financial interests or personal relationships that could have appeared to influence the work reported in this paper.

☒The authors declare the following financial interests/personal relationships which may be considered as potential competing interests:

Serge Suanez reports financial support was provided by the University of Brittany (UBO)

Graphical abstract

Highlights

- The breach opening on gravel spit barrier through cannibalization and rollover processes is decribed
- A method of coastal flooding risk assessment is proposed through modelling of hydrodynamic forcings
- An example of nature-based coastal management is presented as a model for a new regional strategy

The opening of the breach in the proximal part of the Sillon de Talbert took place between the 3rd and 4th of March 2018

Graphics Abstract

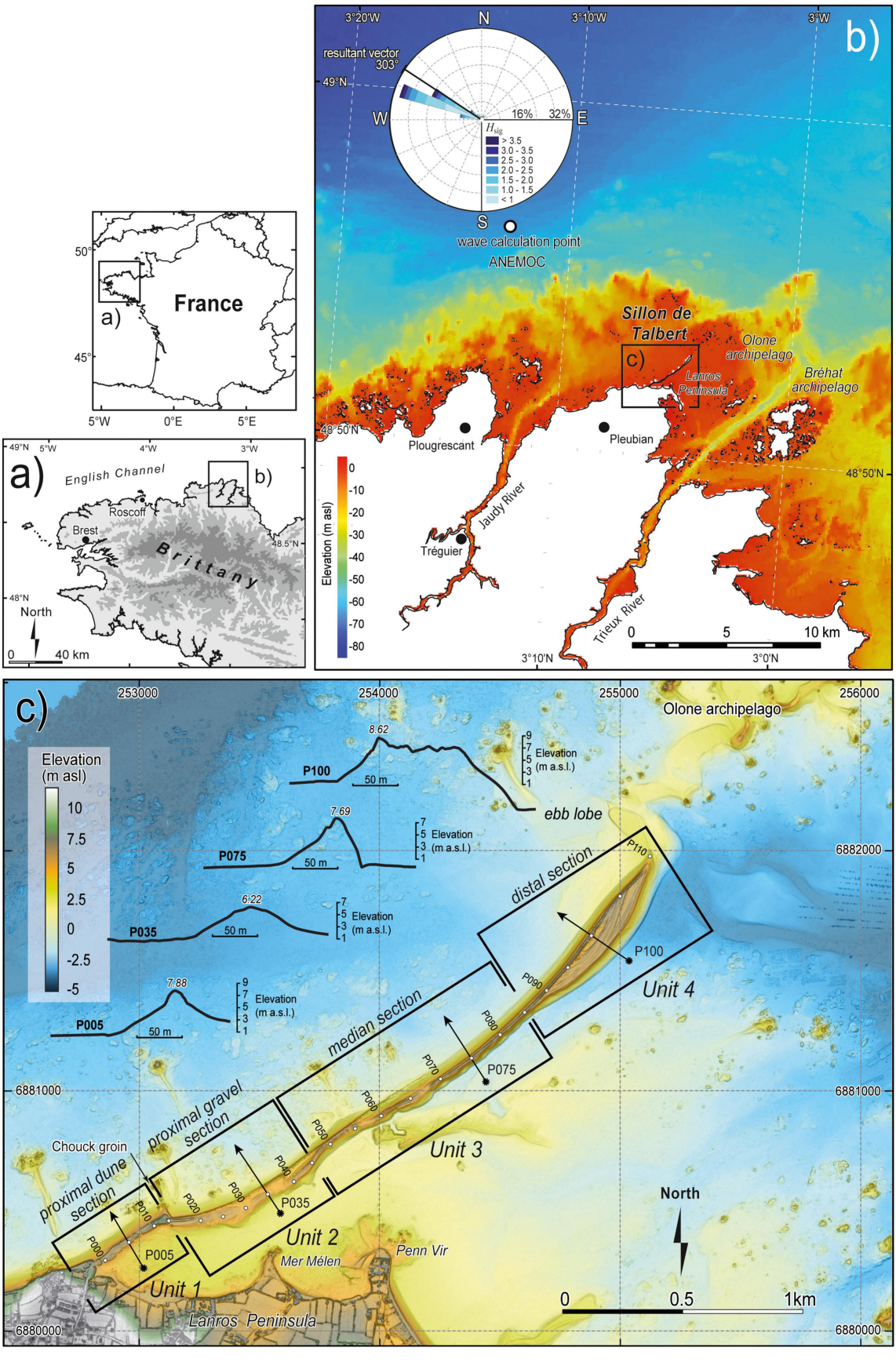
a)
France
50°
45°
5°W
0°E
5°E
b)
English Channel
Roscoff
Brest
Brittany
North
0
40 km
49°N
5°W
4°W
3°W
48.5°N
48°N
3°20'W
3°10'W
3°W
49°N
48°50'N
3°10'N
3°0'N
N
W
E
S
resultant vector
303°
16%
32%
H_{sig}
> 3.5
3.0 - 3.5
2.5 - 3.0
2.0 - 2.5
1.5 - 2.0
1.0 - 1.5
< 1
wave calculation point
ANEMOC
Sillon de Talbert
c)
Olone archipelago
Lanros Peninsula
Bréhat archipelago
Plougrescant
Pleubian
Tréguier
Jaudy River
Trieux River
Elevation (m asl)
0
-10
-20
-30
-40
-50
-60
-70
-80
0
5
10 km
c)
253000
254000
255000
256000
6882000
6881000
6880000
Olone archipelago
Elevation (m asl)
10
7.5
5
2.5
0
-2.5
-5
P100
8.62
50 m
Elevation (m a.s.l.)
ebb lobe
P075
7.69
P035
6.22
P005
7.88
distal section
median section
proximal gravel section
proximal dune section
Chouck groin
Unit 4
Unit 3
Unit 2
Unit 1
Mer Mélen
Penn Vir
Lanros Peninsula
P110
P090
P080
P070
P060
P050
P040
P030
P020
P010
P000
North
0
0.5
1km

Figure 1

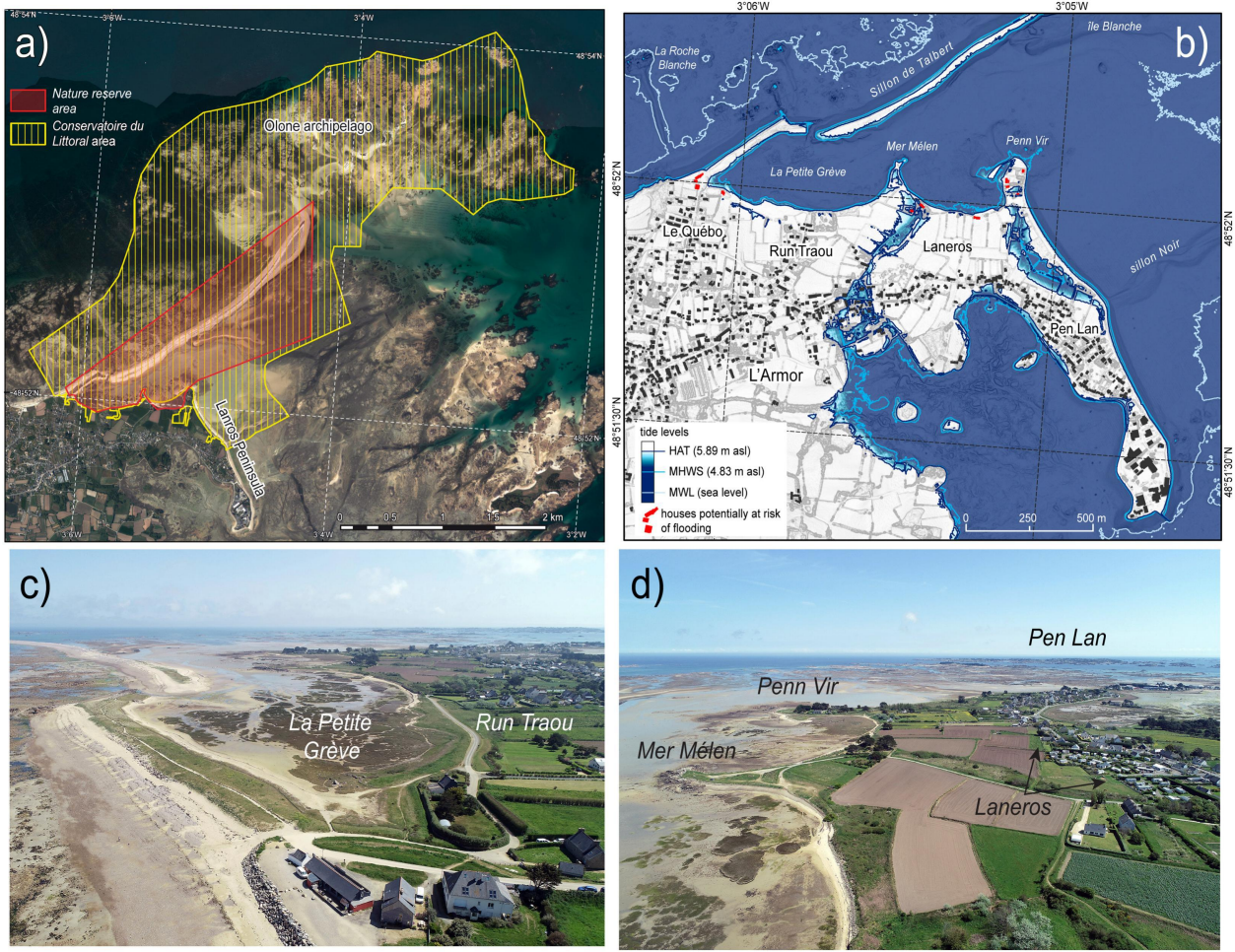
a)
Nature reserve area
Conservatoire du Littoral area
Olone archipelago
Laneros Peninsula
48°54'N
3°6'W
3°4'W
48°52'N
0
0.5
1
1.5
2 km
b)
3°06'W
3°05'W
Ile Blanche
La Roche Blanche
Sillon de Talbert
Mer Mélen
Penn Vir
La Petite Grève
Le Québo
Run Traou
Laneros
sillon Noir
Pen Lan
L'Armor
48°52'N
48°51'30"N
tide levels
HAT (5.89 m asl)
MHWS (4.83 m asl)
MWL (sea level)
houses potentially at risk of flooding
0
250
500 m
c)
La Petite Grève
Run Traou
d)
Pen Lan
Penn Vir
Mer Mélen
Laneros

Figure 2

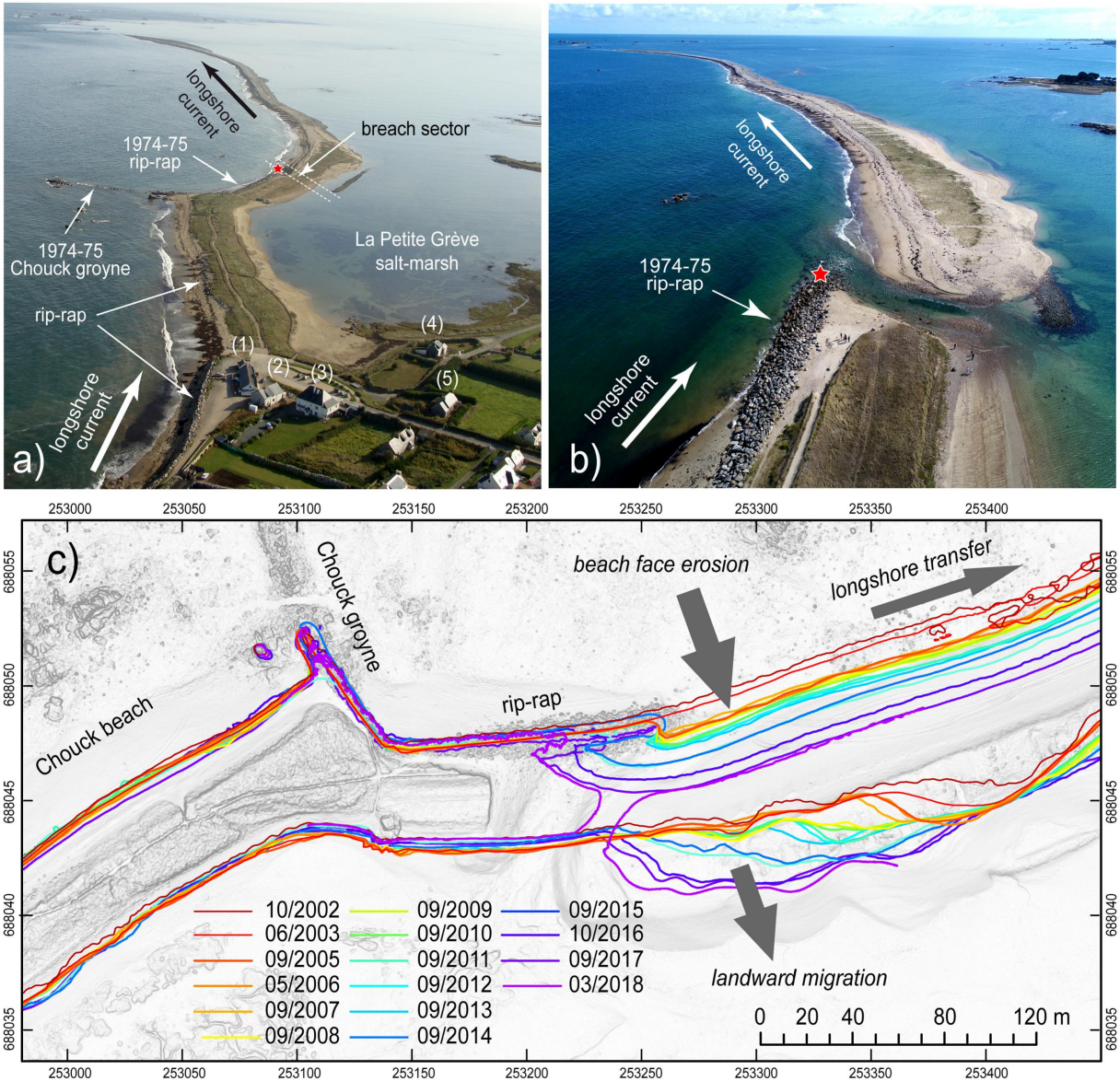
a)
longshore current
1974-75 rip-rap
breach sector
1974-75 Chouck groyne
La Petite Grève salt-marsh
rip-rap
(1)
(2)
(3)
(4)
(5)
longshore current
b)
longshore current
1974-75 rip-rap
longshore current
c)
Chouck groyne
beach face erosion
longshore transfer
Chouck beach
rip-rap
landward migration
10/2002
06/2003
09/2005
05/2006
09/2007
09/2008
09/2009
09/2010
09/2011
09/2012
09/2013
09/2014
09/2015
10/2016
09/2017
03/2018
0 20 40 80 120 m
253000
253050
253100
253150
253200
253250
253300
253350
253400
688055
688050
688045
688040
688035

Figure 3

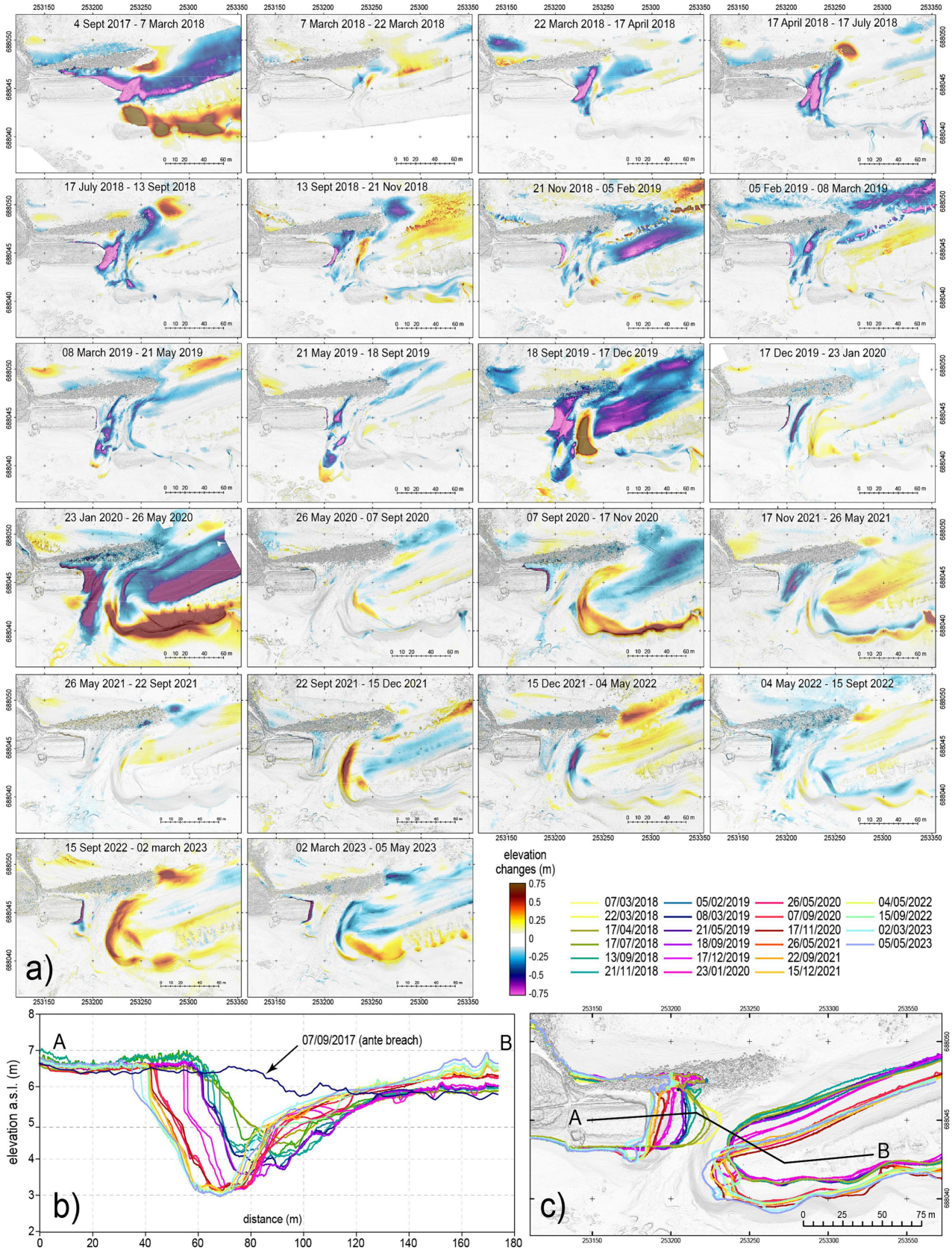
4 Sept 2017 - 7 March 2018
7 March 2018 - 22 March 2018
22 March 2018 - 17 April 2018
17 April 2018 - 17 July 2018
17 July 2018 - 13 Sept 2018
13 Sept 2018 - 21 Nov 2018
21 Nov 2018 - 05 Feb 2019
05 Feb 2019 - 08 March 2019
08 March 2019 - 21 May 2019
21 May 2019 - 18 Sept 2019
18 Sept 2019 - 17 Dec 2019
17 Dec 2019 - 23 Jan 2020
23 Jan 2020 - 26 May 2020
26 May 2020 - 07 Sept 2020
07 Sept 2020 - 17 Nov 2020
17 Nov 2021 - 26 May 2021
26 May 2021 - 22 Sept 2021
22 Sept 2021 - 15 Dec 2021
15 Dec 2021 - 04 May 2022
04 May 2022 - 15 Sept 2022
15 Sept 2022 - 02 march 2023
02 March 2023 - 05 May 2023
a)
elevation changes (m)
0.75
0.5
0.25
0
-0.25
-0.5
-0.75
07/03/2018
22/03/2018
17/04/2018
17/07/2018
13/09/2018
21/11/2018
05/02/2019
08/03/2019
21/05/2019
18/09/2019
17/12/2019
23/01/2020
26/05/2020
07/09/2020
17/11/2020
26/05/2021
22/09/2021
15/12/2021
04/05/2022
15/09/2022
02/03/2023
05/05/2023
A
B
07/09/2017 (ante breach)
elevation a.s.l. (m)
distance (m)
b)
A
B
c)
0 25 50 75 m

Figure 4

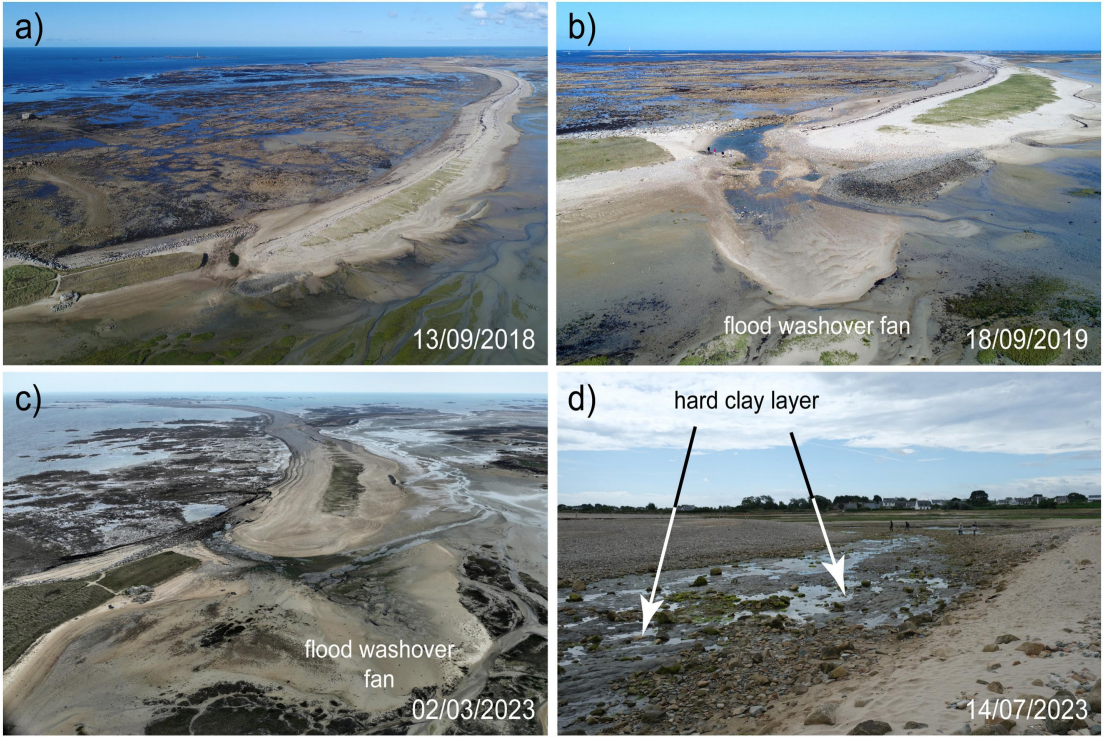
a)
13/09/2018
b)
flood washover fan
18/09/2019
c)
flood washover fan
02/03/2023
d)
hard clay layer
14/07/2023

Figure 5

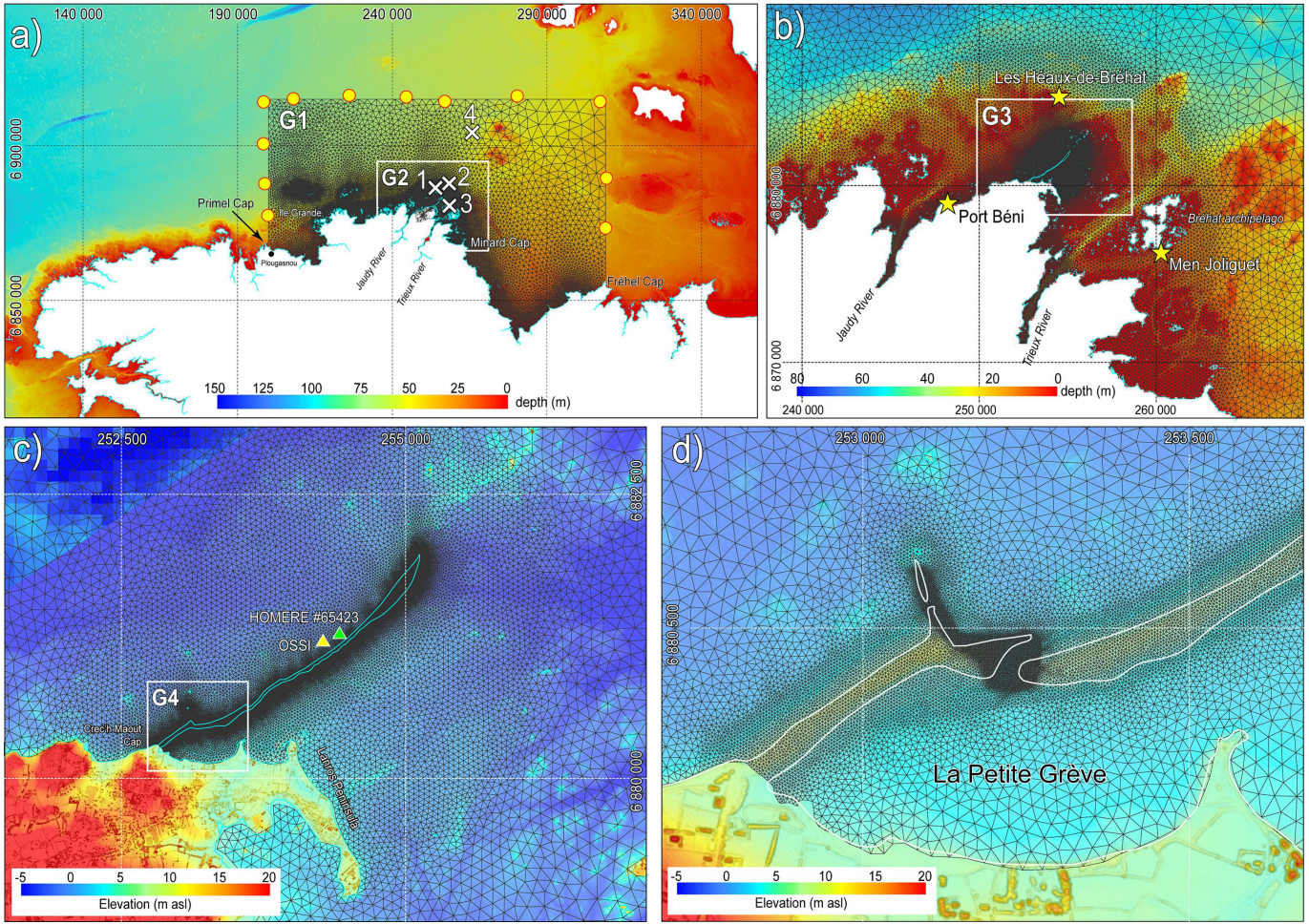
a)
140 000
190 000
240 000
290 000
340 000
6 900 000
6 650 000
G1
G2
1
2
3
4
Primel Cap
Ile Grande
Plougasnou
Jaudy River
Trieux River
Minard Cap
Bréhat Cap
150 125 100 75 50 25 0
depth (m)
b)
Les Heaux-de-Bréhat
G3
Port Béni
Bréhat archipelago
Men Joliguet
Jaudy River
Trieux River
6 890 000
6 870 000
80 60 40 20 0
depth (m)
240 000
250 000
260 000
c)
252 500
255 000
6 882 500
6 880 000
HOMERE #65423
OSSI
G4
Crech Maout Cap
Larros Peutissile
-5 0 5 10 15 20
Elevation (m asl)
d)
253 000
253 500
6 880 500
La Petite Grève
-5 0 5 10 15 20
Elevation (m asl)

Figure 6

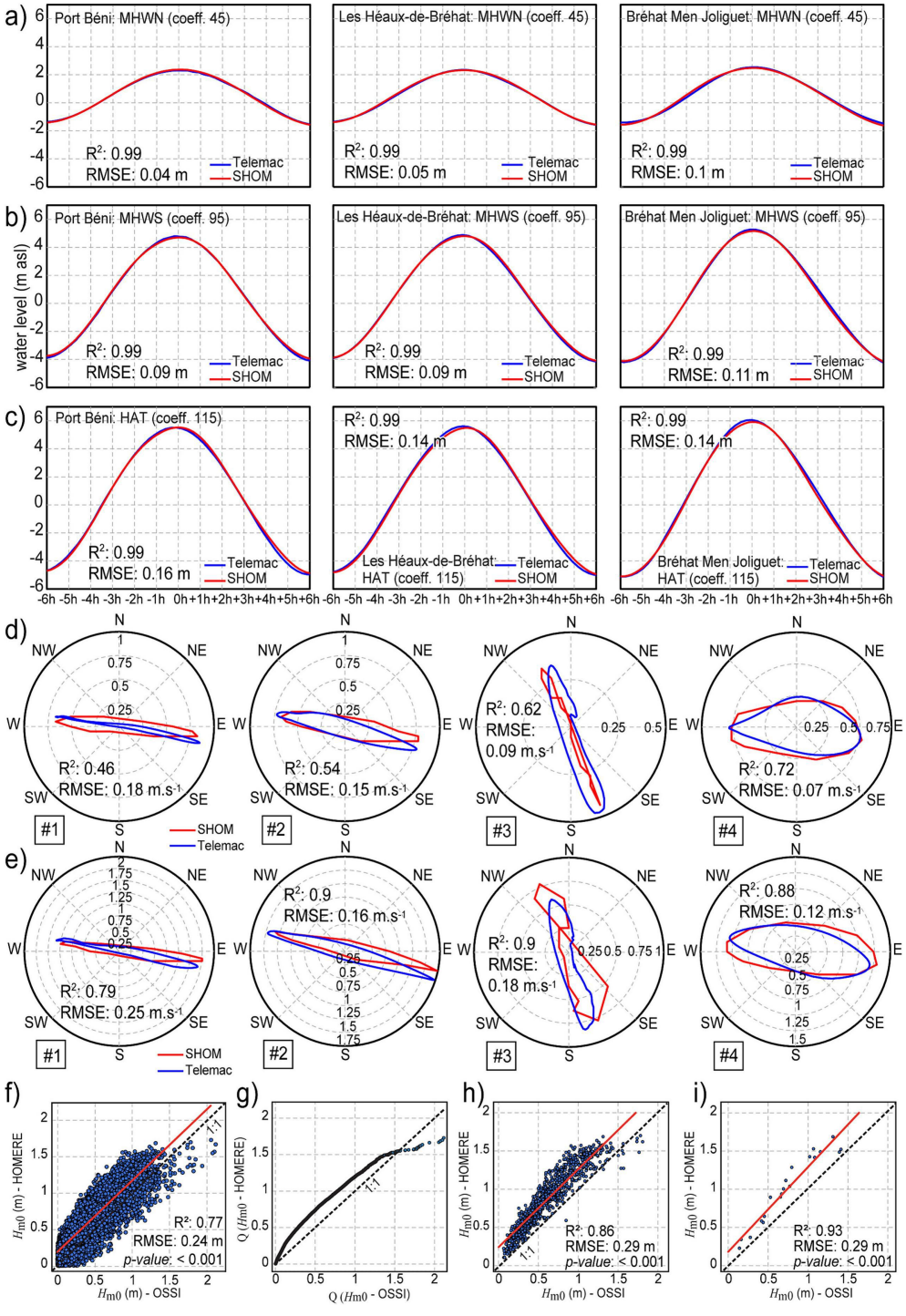
a)
Port Béni: MHWN (coeff. 45)
R²: 0.99
RMSE: 0.04 m
Telemac
SHOM
Les Héaux-de-Bréhat: MHWN (coeff. 45)
R²: 0.99
RMSE: 0.05 m
Telemac
SHOM
Bréhat Men Joliguet: MHWN (coeff. 45)
R²: 0.99
RMSE: 0.1 m
Telemac
SHOM
b)
water level (m asl)
Port Béni: MHWS (coeff. 95)
R²: 0.99
RMSE: 0.09 m
Telemac
SHOM
Les Héaux-de-Bréhat: MHWS (coeff. 95)
R²: 0.99
RMSE: 0.09 m
Telemac
SHOM
Bréhat Men Joliguet: MHWS (coeff. 95)
R²: 0.99
RMSE: 0.11 m
Telemac
SHOM
c)
Port Béni: HAT (coeff. 115)
R²: 0.99
RMSE: 0.16 m
Telemac
SHOM
R²: 0.99
RMSE: 0.14 m
Les Héaux-de-Bréhat:
HAT (coeff. 115)
Telemac
SHOM
R²: 0.99
RMSE: 0.14 m
Bréhat Men Joliguet:
HAT (coeff. 115)
Telemac
SHOM
-6h -5h -4h -3h -2h -1h 0h+1h+2h+3h+4h+5h+6h
d)
R²: 0.46
RMSE: 0.18 m.s-1
#1
R²: 0.54
RMSE: 0.15 m.s-1
#2
R²: 0.62
RMSE:
0.09 m.s-1
#3
R²: 0.72
RMSE: 0.07 m.s-1
#4
SHOM
Telemac
e)
R²: 0.79
RMSE: 0.25 m.s-1
#1
R²: 0.9
RMSE: 0.16 m.s-1
#2
R²: 0.9
RMSE:
0.18 m.s-1
#3
R²: 0.88
RMSE: 0.12 m.s-1
#4
SHOM
Telemac
f)
Hm0 (m) - HOMERE
Hm0 (m) - OSSI
1:1
R²: 0.77
RMSE: 0.24 m
p-value: < 0.001
g)
Q (Hm0 - HOMERE)
Q (Hm0 - OSSI)
1:1
h)
Hm0 (m) - HOMERE
Hm0 (m) - OSSI
1:1
R²: 0.86
RMSE: 0.29 m
p-value: < 0.001
i)
Hm0 (m) - HOMERE
Hm0 (m) - OSSI
R²: 0.93
RMSE: 0.29 m
p-value: < 0.001

Figure 7

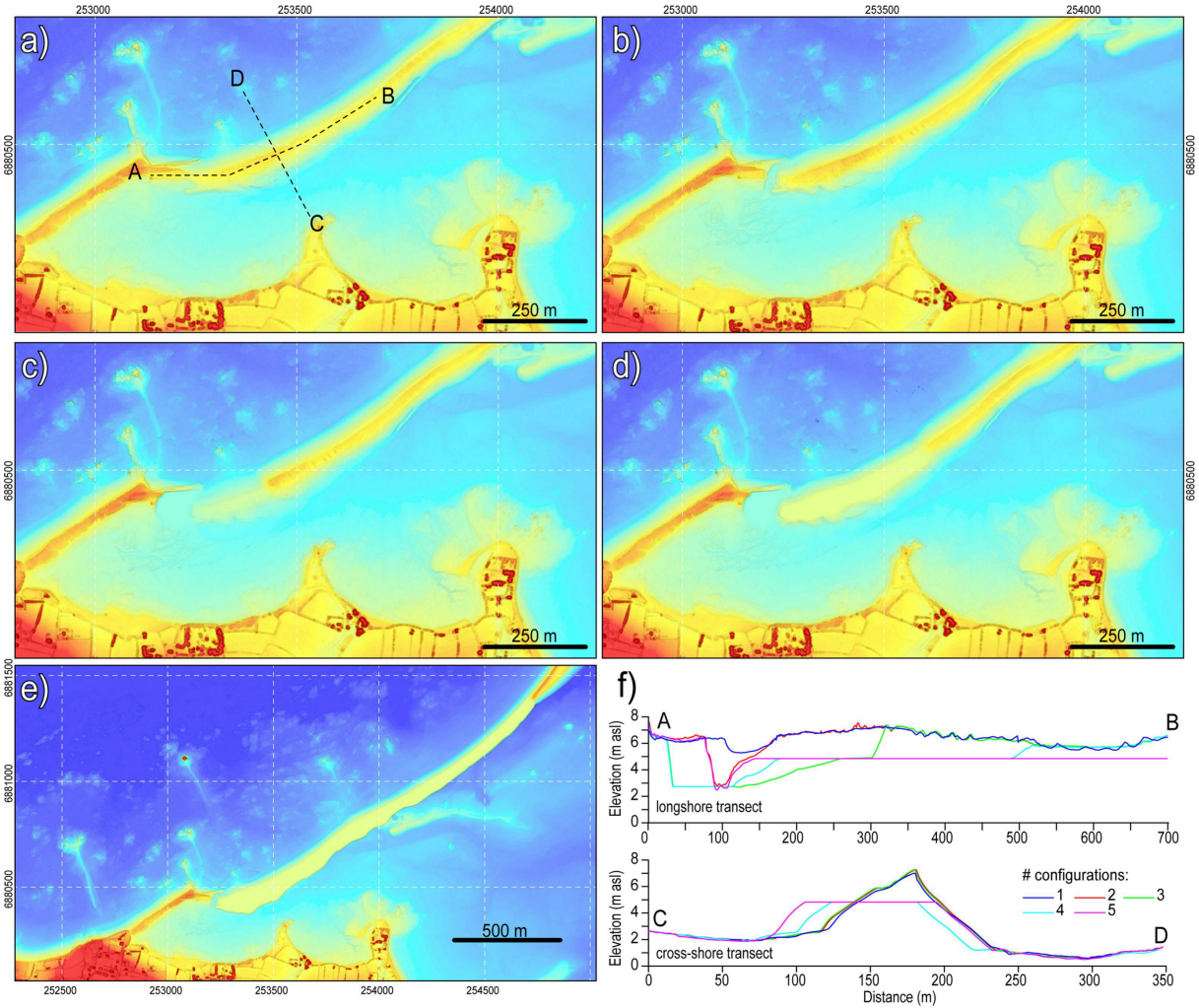
a)
b)
c)
d)
e)
f)
A
B
C
D
250 m
500 m
253000
253500
254000
252500
254500
6880500
6881000
6881500
Elevation (m asl)
longshore transect
cross-shore transect
configurations:
1
2
3
4
5
Distance (m)

Figure 8

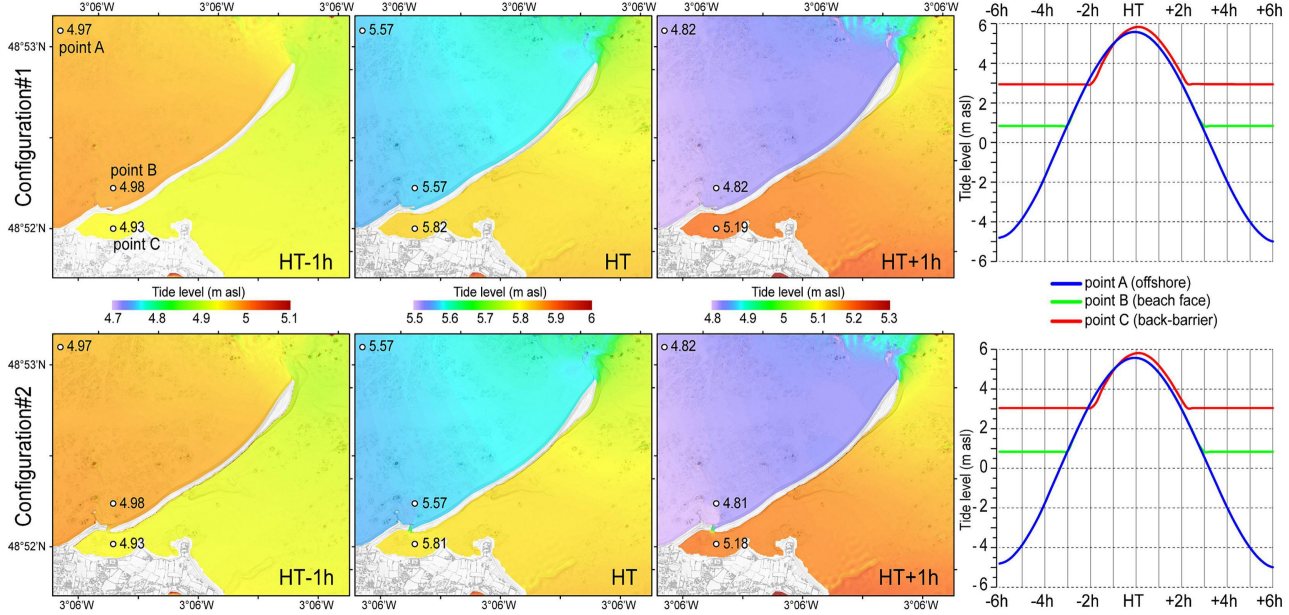
Configuration#1
Configuration#2
3°06'W
48°53'N
48°52'N
point A
point B
point C
4.97
4.98
4.93
5.57
5.82
4.82
5.19
4.81
5.18
5.81
HT-1h
HT
HT+1h
Tide level (m asl)
4.7 4.8 4.9 5 5.1
5.5 5.6 5.7 5.8 5.9 6
4.8 4.9 5 5.1 5.2 5.3
-6h -4h -2h HT +2h +4h +6h
Tide level (m asl)
point A (offshore)
point B (beach face)
point C (back-barrier)

Figure 9

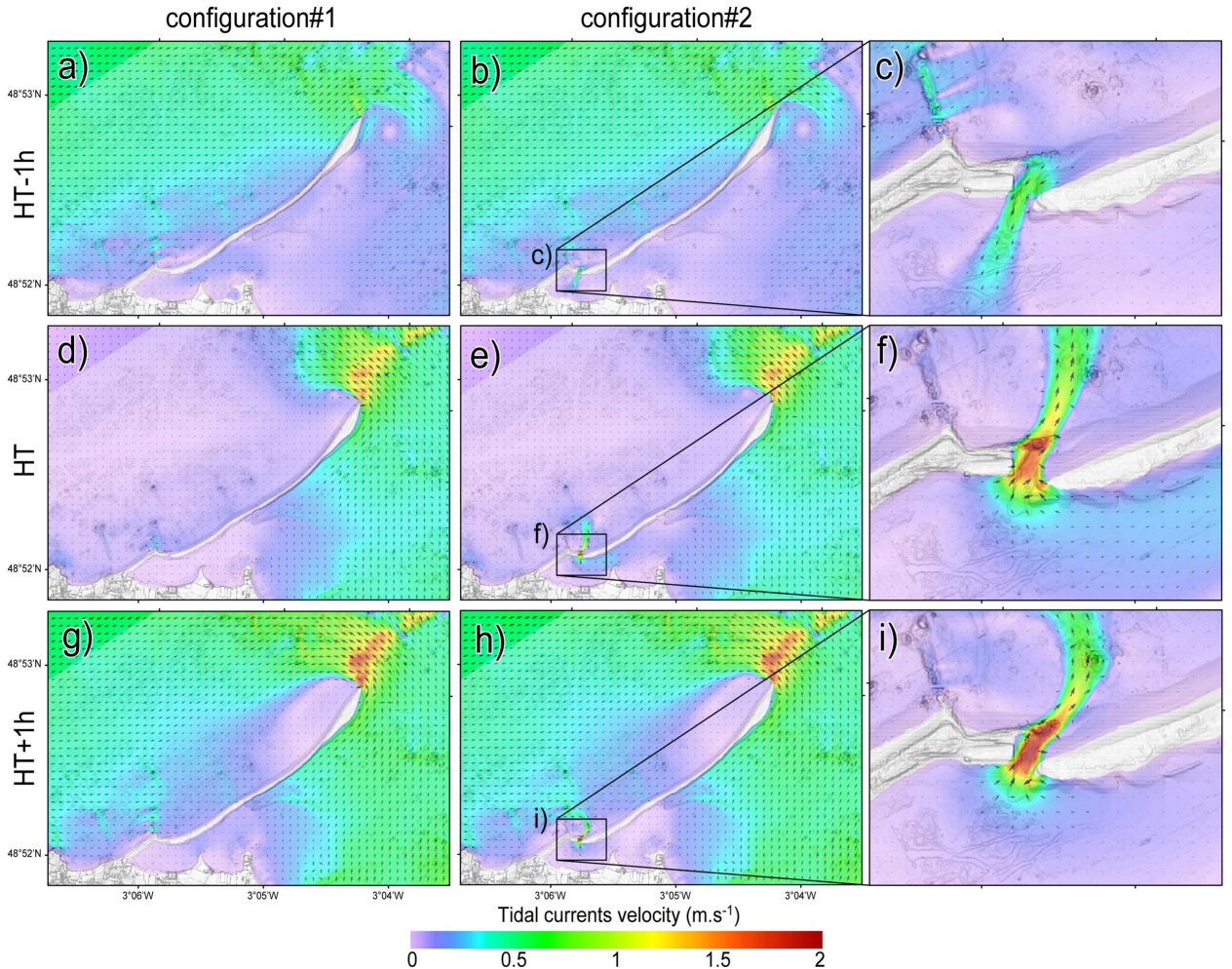
configuration#1
configuration#2
a)
b)
c)
d)
e)
f)
g)
h)
i)
HT-1h
HT
HT+1h
48°53'N
48°52'N
3°06'W
3°05'W
3°04'W
Tidal currents velocity (m.s-1)
0
0.5
1
1.5
2

Figure 10

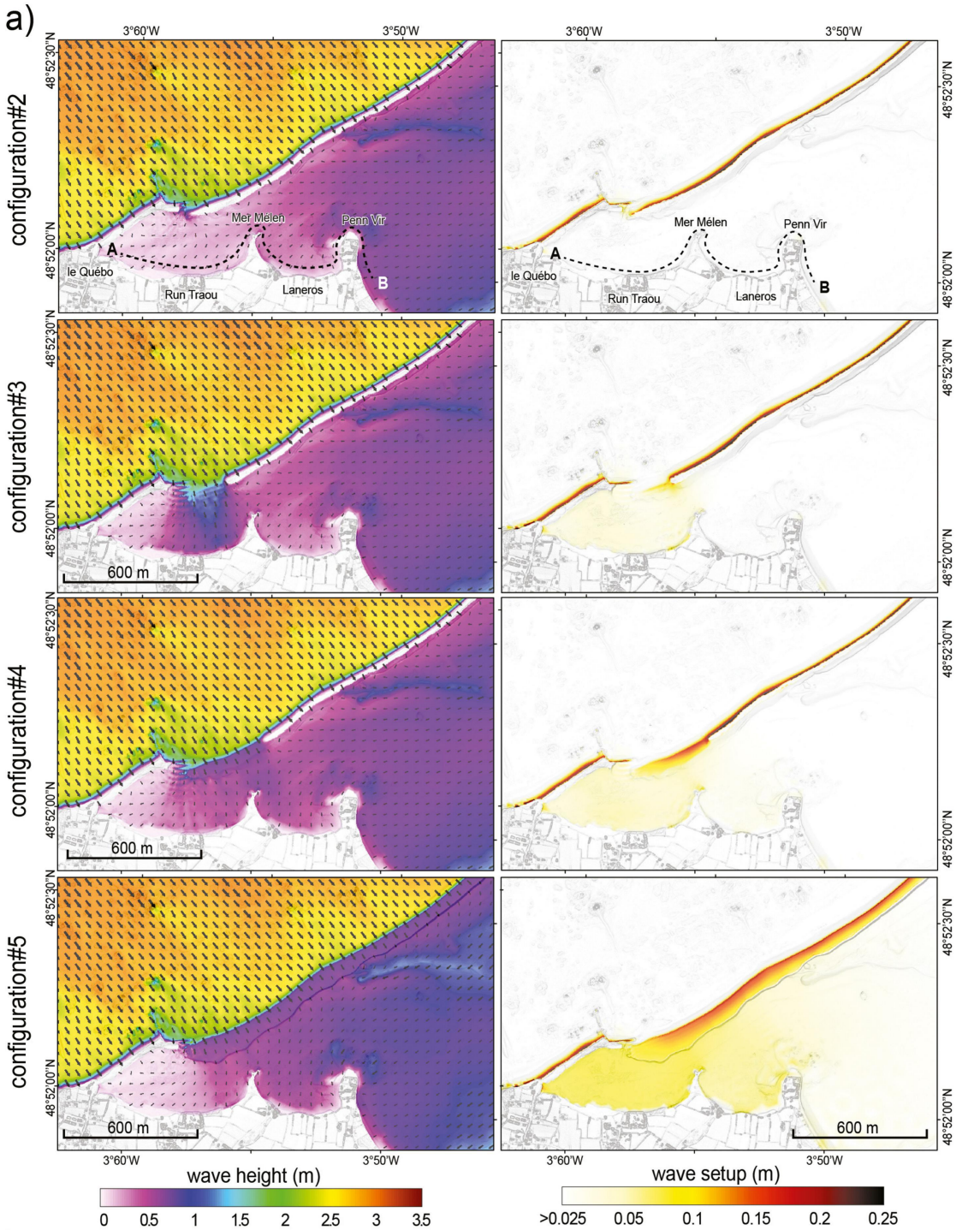
a)
configuration#2
configuration#3
configuration#4
configuration#5
3°60'W
3°50'W
48°52'30"N
48°52'00"N
Mer Mélen
Penn Vir
A
B
le Québo
Run Traou
Laneros
600 m
wave height (m)
0
0.5
1
1.5
2
2.5
3
3.5
wave setup (m)
>0.025
0.05
0.1
0.15
0.2
0.25

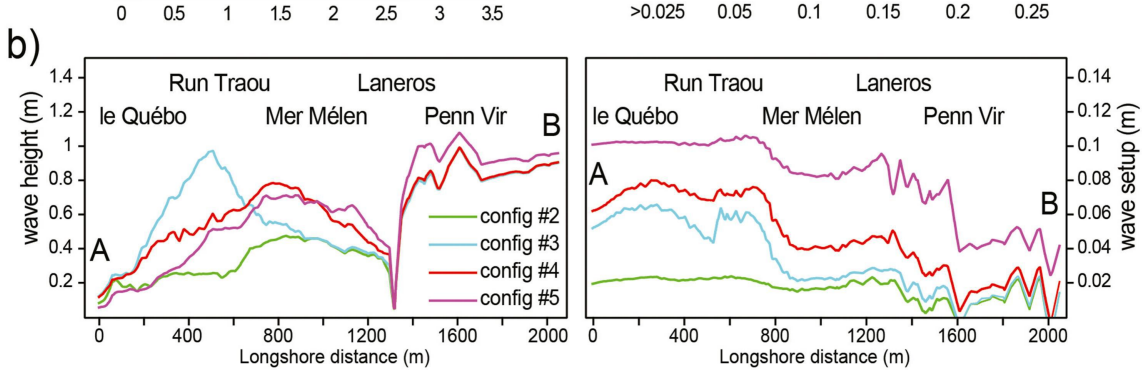
b)
Run Traou
Laneros
le Québo
Mer Mélen
Penn Vir
A
B
wave height (m)
wave setup (m)
config #2
config #3
config #4
config #5
Longshore distance (m)
0
400
800
1200
1600
2000

Figure 11

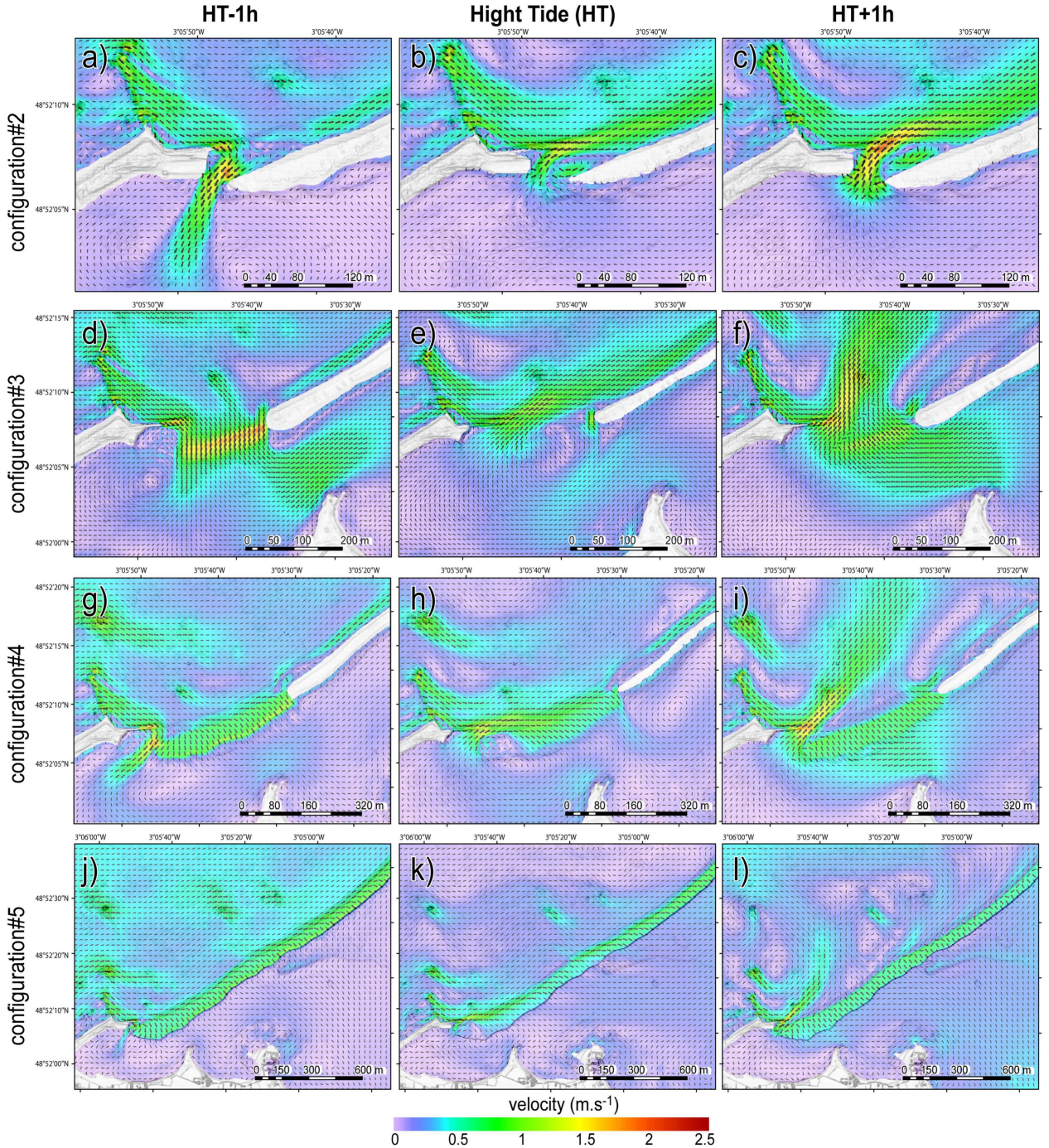
HT-1h
Hight Tide (HT)
HT+1h
configuration#2
configuration#3
configuration#4
configuration#5
a)
b)
c)
d)
e)
f)
g)
h)
i)
j)
k)
l)
0 40 80 120 m
0 50 100 200 m
0 80 160 320 m
0 150 300 600 m
velocity (m.s-1)
0 0.5 1 1.5 2 2.5

Figure 12

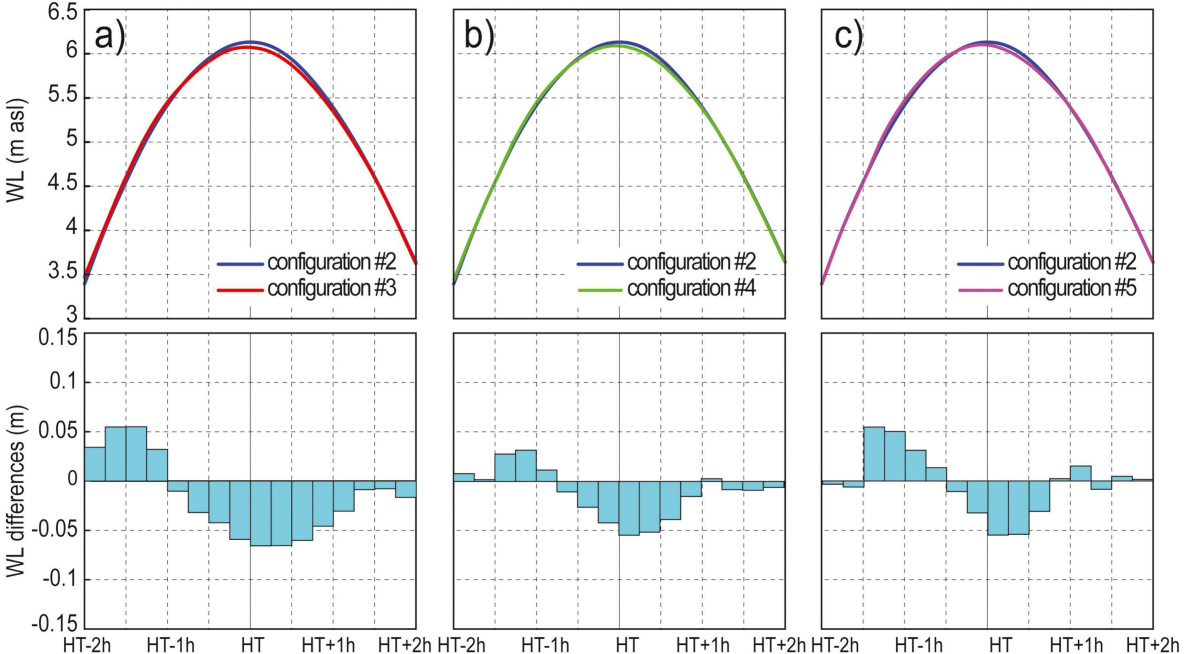
a)
b)
c)
WL (m asl)
6.5
6
5.5
5
4.5
4
3.5
3
configuration #2
configuration #3
configuration #4
configuration #5
WL differences (m)
0.15
0.1
0.05
0
-0.05
-0.1
-0.15
HT-2h
HT-1h
HT
HT+1h
HT+2h

Figure 13